Saturation of vorticity growth in fully-developed fluid turbulence

A Thesis
Submitted for the Degree of
Master of Science (Engineering)

by

Chakradhar Thantanapally

Engineering Mechanics Unit
Jawaharlal Nehru Centre for Advanced Scientific Research
(A Deemed University)
Bangalore – 560 064

AUGUST 2013

My Parents and Grandparents

DECLARATION

I hereby declare that the matter embodied in the thesis entitled "**Saturation of vorticity growth in fully-developed fluid turbulence**" is the result of investigations carried out by me as a student of the Engineering Mechanics Unit, Jawaharlal Nehru Centre for Advanced Scientific Research, Bangalore, India under the supervision of **Dr. Santosh Ansumali** and that it has not been submitted elsewhere for the award of any degree or diploma.

In keeping with the general practice in reporting scientific observations, due acknowledgment has been made whenever the work described is based on the findings of other investigators.

Chakradhar Thantanapally

CERTIFICATE

I hereby certify that the matter embodied in this thesis entitled "**Saturation of vorticity growth in fully-developed fluid turbulence**" has been carried out by **Mr. Chakradhar Thantanapally** as a student of the Engineering Mechanics Unit, Jawaharlal Nehru Centre for Advanced Scientific Research, Bangalore, India under my supervision and that it has not been submitted elsewhere for the award of any degree or diploma.

Dr. Santosh Ansumali
(Research Supervisor)

Acknowledgements

I would like to thank my advisor *Dr. Santosh Ansumali* for his motivation, guidance and immense support which has made this thesis possible. I thank him for the personal care that he has shown towards me from the beginning, his enormous patience and all the painstakingly sleepless nights that he spent with the group in coding and debugging. *Prof. Sauro Succi* for the scientific discussions which forms a substantial part of this thesis. His motivation and valuable advice both in academics and career helped me a great deal in shaping my future.

Prof. Roddam Narasimha, Prof. V. Kumaran, Prof. Rahul Pandit for the discussions, suggestions and comments on my work. *Radio (Subrahmanyam)* without whose advice I wouldn't have joined JNC. His inspiration, outlook and guidance has been an immense value for me. EMU faculty especially *Prof. Ganesh Subramanian* for his rigorous (both physical arguments and mathematical derivations) lectures in fluid mechanics. *Prof. K. R. Sreenivas* for the technical discussions during the coursework. *Prof. Rama Govindarajan* for the lively class room atmosphere which I enjoyed the most.

My *parents* and *grandparents* for their constant support throughout. My brother for supporting all my endeavors. *Prathyush* for being my constant source of motivation and all the endless conversations related to psychology and philosophy. *Anu* for the emotional support and special relation that we share. *Karthi, Kalyan, Dep, Reddy, Mihi, Nanda, Wall* for their cherishing friendship.

Siddharth for all the friendly chats regarding insti and other matters in comfortable insti lingo. LB coding without his help would have been a very difficult task. *Shiwani* for helping me through various LB concepts. *Dr. Dhiraj Patil* for the collaborative work. EMU-mates - *Ponnu, Dhiraj, Jose, Deepthi, Deepak, PP, Navaneeth, Sai Kishan, Aarthi, Manjusha, Rashmi, Shahajhan, Reddy, Rajesh, Rohith, Ujjain(Hermite), Ramki, Saikat, Vicky, Sankalp, Reddy. Jr, Chandu, Sai, Aman*, who are responsible for an energetic and sound departmental environment, discussing and fighting over diversified topics related to academics, sports, politics, other department issues etc. 'Friends' sessions with PP and Deepthi.

I'm grateful to my friends- *Hegde, Sharmila, Anjali, Ananthu, Meha* who are always there for me equally through highs and lows. For all the good times we had together which made my stay in JNC a memorable experience. Cooking sessions with *Priyanka*. Evening walks, bird watching, photography, cycling and Gym companion *Vybhav*. Bike trips with Kanwar(the flying Sikh). Other friends - Croor, Meenakshi, Sunil, Shashank, Nisha for the fun times together. Foot ball community for the wonderful evenings. *Sivani, Diwakar, Malli* for the trips and good times in JNC during my first year. *Milli* for introducing me to guitar, spending his time patiently teaching all the basics. *Pink Floyd* and *Led Zeppelin* for being my source of energy especially during late hours of my work.

Intel for providing the computational resources and travel grant for my conference. I thank the administrative officer *Jayachandra*, *admin*, *library* and *complab* staff, *Vijayalakshmi*, *Harisha*, *Princy* for their help from time to time. Finally, I thank JNCASR and DST for providing all the financial and infrastructural support to pursue my MS here.

Abstract

In present thesis, using large scale computations, universal features in the transient dynamics towards steady state turbulence is investigated. In particular, via simulations of transient decaying three-dimensional flows, it is suggested that the saturation of vorticity growth takes place through the onset of transient, and yet universal, appearance of $k^{-3}\left(\log\left(k/k_0\right)\right)^n$ spectrum, where $k_0 \sim 3$ and $n \sim 1$. This is indeed confirmed with three different initial conditions of Kida-Pelz, Taylor-Green and a set of Hill's vortices. The results of numerical simulations, in the transient, are reported up to a Reynolds number of 10^4 and grid resolution of 1536^3. This is a comparatively less studied aspect of turbulence, perhaps due to the fact that universal behavior is usually associated to time-asymptotic states, whereas transient features, being driven by morphological details, are typically regarded as inherently non-universal.

These simulations were performed by using two set of tools: the pseudo-spectral (PS) and multi-relaxation time version of Lattice Boltzmann methods (LB). The former has served as the workhorse of homogeneous incompressible turbulence for the last four decades, and is widely described in the literature. The latter is a more recent real-space kinetic method, based on a minimal lattice formulation of the Boltzmann kinetic equation. The Lattice Boltzmann method is an attractive option for the direct numerical simulation of turbulent flows, due to its high parallel scalability and ease of application to complex geometries. The physical phenomena discussed in the main text has been initially observed with the LB simulation and is later confirmed using the PS simulations.

However, unlike conventional methods, such as PS for Navier-Stokes, grid-resolution requirements and accuracy of the LBM for direct numerical simulations, have been thoroughly tested for a few setups only. Furthermore, it is empirically known that compressibility-related errors may lead to poor comparison between PS and LBM at moderate grid-sizes. In the second part of thesis, the aim is to investigate the limit up to which LB method can be used in subgrid simulations. In particular effect of collision models was investigated and it was shown that multi-relaxation LBM with tunable Prandtl number is efficient in damping acoustic oscillations uniformly both in sub-grid as well as high resolution simulations.

List of Figures

List of Tables

Contents

Chapter 1

Introduction

Transient universality

Turbulence can be defined as that state of matter characterized by a loss of coherence in space and time, as a result of the non-linear interaction of a large number of degrees of freedom, in excess of billions even for most familiar phenomena, such as flow past an automobile (Frisch 1995; Chen *et al.* 2003; Davidson 2004). This raises a formidable computational barrier even for the most powerful computational methods in the foreseeable future, let alone analytical methods. It is therefore not surprising that fluid turbulence has continued to attract attention by scientists from many disciplines. The research and literature on the topic is so vast that even the problem definition is not the same for different communities of researchers (Sreenivasan 1999; Frisch 1995; Liepmann 1979; Pope 2000; Lumley & Yaglom 2001). Among others, primary goals of turbulence research can be summarized as follows: i) unveil statistical universalities (Frisch 1995; Sreenivasan & Antonia 1997; Toschi & Bodenschatz 2009; Dhar *et al.* 1997), underlying the irreducible dynamical complexity of different turbulent flows, ii) develop robust and accurate methods to compute the (statistical) dynamics of turbulent flows (Moin & Mahesh 1998; Germano 1992; Lesieur & Metais 1996; Ansumali *et al.* 2004; Moin & Mahesh 1998) in realistic geometries, where universal and non-universal behavior must necessarily coexist, and iii) understanding the basic mechanisms controlling the transition from laminar to turbulent behavior (Sreenivasan 1999; Moxey & Barkley 2010).

This thesis contains two parts : In the first part a pseudo-spectral code is developed and is used to investigate theoretical questions in decaying turbulence. In the second part a lattice Boltzmann framework is refined using benchmark data from pseudo-spectral method.

In this thesis, numerical results from large-scale, long-time, simulations of decaying homogeneous turbulence are reported, which indicate that blowup of inviscid flows is tamed by the emergence of collective dynamics of coherent structures. The simulations performed also suggest that this collective dynamics might lead to universal behavior during the transient evolution of turbulence. To date, such universality was mostly associated with time-asymptotic states, whereas transient features, being driven by morphological details, were typically regarded as inherently non-universal. In particular, simulations with three different initial conditions, show evidence of a $k^{-3}\log k$ spectrum in the transient stage, before the Kolmogorov $k^{-5/3}$ asymptotic regime is attained. Such universal transient might serve as a spectral funnel to the time-asymptotic Kolmogorov spectrum, which is invariably observed in the late stage of all three simulations presented in this work. The present work is entirely based on simulation evidence. However, the statistical analysis of the coherent structures suggests an analogy with population dynamics, which might be conducive to new mathematical models of transient decaying turbulence.

Quasi-equilibrium lattice Boltzmann method

The Lattice Boltzmann (LB) method is an attractive option for the direct numerical simulation of turbulent flows, due to its high parallel scalability and ease of application to complex geometries (Benzi *et al.* 1992; Chen & Doolen 1998; Succi 2001; Yu & Girimaji 2005, 2006). However, unlike conventional methods, such as pseudo-spectral (PS) for Navier-Stokes (Canuto *et al.* 1988), grid-resolution requirements and accuracy of the LB method for DNS, have been thoroughly tested for a few setups only(Bespalko 2011). Furthermore, it is empirically known that compressibility-related errors may lead to poor comparison between PS and LBM at moderate grid-sizes(Peng *et al.* 2010). At this point, we would also like to remind that in sub-grid domain, multiple relaxation models with high bulk viscosity often perform better than single relaxation models, which exhibit no bulk viscosity. The typical interpretation for such a behavior is that, in the sub-grid domain, acoustic oscillations can be effectively suppressed by high bulk viscosity(Asinari & Karlin 2010). In this work we show that, motivated via multi-relaxation LB method using a tunable Prandtl number, spurious acoustic fluctuations are efficiently damped in comparison to tunable bulk viscosity model. The main idea is to increase the stability in sub-grid domain and accuracy in well resolved domains tuning the Prandtl number. The aim is to push LB code for hydrodynamics as closer in accuracy as possible, compared to PS code.

The chapters of this thesis are arranged as follows

- **Chapter 2 : Pseudo-spectral method** In this chapter, pseudo-spectral method that is used as a simulation tool to study homogeneous turbulence is described. Space discretization and time marching schemes used for the simulations are detailed.
- **Chapter 3 : Universal mechanism for saturation of vorticity growth** This chapter reports the energy scaling laws and statistical analysis around the transient region where peak in maximum vorticity is obtained. Several observations and possible universalities in the transient dynamics are discussed.
- **Chapter 4 : Quasiequilibrium lattice Boltzmann models** A novel approach to multi-relaxation LB method using tunable Prandtl number is formulated. This is achieved by introducing a quasi-equilibrium state before attaining the final equilibrium. Two-dimensional and three-dimensional results supporting the claim are given.
- **Chapter 5 : Summary and conclusions** A brief summary and conclusion of this thesis work is provided in this chapter.
- **Appendix :** Details of the computational resources used for the simulations is provided.

Chapter 2

Pseudo-spectral method

Pseudo spectral methods are standard tools for the direct numerical simulation (DNS) of homogeneous turbulence. The trial functions for spectral methods are infinitely differentiable global functions. The expansion of a function in terms of an infinite sequence of orthogonal functions $\{\phi_k\}, u = \sum_{k=-\infty}^{\infty} \hat{u}_k \phi_k$, underlies numerical methods of approximation based on PS methods. The expansion in terms of an orthogonal system introduces a linear transformation between u and the sequence of its expansion coefficients $\{\hat{u}_k\}$. In a Fourier expansion, the k^{th} coefficient of the expansion decays faster than any inverse power of k when the function is infinitely smooth and all its derivatives are periodic as well. In practice this decay is not exhibited until there are enough coefficients to represent all the essential structures of the function. The subsequent rapid decay of the coefficients implies that the Fourier series truncated after just a few more terms represents an exceedingly good approximation of the function. This characteristic is usually referred to as "*spectral accuracy*" of the Fourier method. It is also known as *exponential convergence* and *infinite-order accuracy* (Canuto *et al.* 1988). One of the distinguishing features of spectral methods is the calculation of derivative in Fourier space, which is just multiplication of the Fourier coefficients by '$\imath k$', where $\imath = \sqrt{-1}$ and k is the wave number. The difficulty with the calculation of convolution sum of non-linear term is addressed by Orszag (Orszag 1971) using transform methods which has removed the computational head which has led to improved applications in fluid dynamics, meteorology etc. The most familiar approximation results are those for periodic functions expanded in Fourier series.

In this chapter, we review the the implementation details of the pseudo-spectral method that is used to perform the DNS results presented in subsequent chapters. Section 2.1 discusses the discrete Fourier transforms and the fast Fourier transforms (FFT). Section 2.2 briefs about the FFT library used and an in-house library called Panini. Finally in section 2.3time integration schemes used and discretization of governing equations are discussed. Finally, we summarize in section 2.4.

2.1 Discrete Fourier transforms and FFT

We consider a domain of length 2π divided into N number of equispaced points

$$x_j = \frac{2\pi j}{N} \qquad j = 0, 1, ..., N-1 \tag{2.1}$$

On such a grid, starting from function values at these discrete nodes $u(x_j) = u_j$, one defines the discrete Fourier transform(DFT) $\hat{u}_k$ as

$$\hat{u}_k = \frac{1}{N}\sum_{j=0}^{N-1} u_j e^{\imath k x_j} \qquad k = -N/2, ..., N/2 - 1. \tag{2.2}$$

Here, we remind that similar to continuous Fourier transform we have discrete orthogonality relation as

$$\sum_{k=-N/2}^{N/2-1} e^{-\imath k x_p} e^{\imath k x_q} = \begin{cases} N & \text{if p = q } \pm \text{ nN}, \quad \text{n = 0, 1, 2} \cdots \\ 0 & \text{else} \end{cases} \tag{2.3}$$

which allow us to define the inverse transform as

$$u_j = \sum_{k=-N/2}^{N/2-1} \hat{u}_k e^{-\imath k x_j} \qquad j = 0, ..., N - 1. \tag{2.4}$$

Multi-dimensional sums can be evaluated by factoring the three-dimensional basis functions into a product of three one-dimensional functions. The DFT, equation 2.2, can also be written as

$$\hat{u}_k = \frac{1}{N}\sum_{j=0}^{N-1} u_j W^{jk}, \qquad -\frac{N}{2} \le k \le \frac{N}{2} - 1, \tag{2.5}$$

where $W = e^{\frac{2\pi\imath}{N}}$ This expression in matrix notation is

$$\begin{pmatrix} \hat{u}_{-N/2} \\ \hat{u}_{-N/2+1} \\ \vdots \\ \hat{u}_{N/2-1} \end{pmatrix} = \frac{1}{N} \begin{pmatrix} 1 & W^{-N/2} & \cdots & W^{(-N/2)(N-1)} \\ 1 & W^{-N/2+1)} & \cdots & W^{(-N/2+1)(N-1)} \\ \vdots & & & \vdots \\ 1 & W^{(N/2-1)} & \cdots & W^{(N/2-1)(N-1)} \end{pmatrix} \begin{pmatrix} u_0 \\ u_1 \\ \vdots \\ u_N \end{pmatrix}$$

From this matrix-vector representation, it is evident that a naive implementation would require O(N^2) operations. A key feature of DFT is that the Fourier transform of derivative Du_j (where D $\equiv \frac{\partial}{\partial x}$) of a function u_j is

$$Du_j = -\imath k \sum_{k=-N/2}^{N/2-1} \hat{u}_k e^{-\imath k x_j} \qquad j = 0, ..., N - 1. \tag{2.6}$$

In other words taking derivative in Fourier space changes to a simple matrix multiplication

$$\begin{pmatrix} -\imath(-N/2) & 0 & \cdots & 0 \\ 0 & -\imath(-N/2+1) & \cdots & 0 \\ \vdots & & & \vdots \\ 0 & 0 & \cdots & \imath(N/2-1) \end{pmatrix} \begin{pmatrix} \hat{u}_{-N/2} \\ \hat{u}_{-N/2+1} \\ \vdots \\ \hat{u}_{N/2-1} \end{pmatrix}$$

However, an evaluation of non-linear or variable-coefficient problems requires evaluation of

convolution sums. For example, consider a quadratic function $w(x) = u(x)v(x)$ of some functions u(x) and v(x), the nonlinear term w(x) when expanded in Fourier series is a convolution sum given by (Canuto *et al.* 1988; Boyd 2001)

$$\hat{w}_k = \sum_{m+n=k;\,|m|,|n|\leq N/2} \hat{u}_m \hat{v}_n \qquad k = -N/2, ..., N/2 - 1 \tag{2.7}$$

where u(x), v(x) approximated by their respective truncated Fourier series of degree N/2 is

$$\begin{aligned} \hat{u}_k &= \frac{1}{N} \sum_{j=0}^{N-1} u_j e^{\imath k x_j} \qquad k = -N/2, ..., N/2 - 1, \\ \hat{v}_k &= \frac{1}{N} \sum_{j=0}^{N-1} v_j e^{\imath k x_j} \qquad k = -N/2, ..., N/2 - 1. \end{aligned} \tag{2.8}$$

The direct summation takes $O(N^2)$ operations, where as in three dimensions, the cost is $O(N^4)$. This is prohibitively expensive, especially when one considers that for a non-linear term a finite-difference algorithm takes $O(N)$ operations in one dimension and $O(N^3)$ in three dimensions.

2.1.1 FFT

For simplicity in a DFT, if N is even , we can split $\{u_j\}$ into two sequences of length N/2 which has even and odd coefficients respectively, given by

$$\begin{aligned} \hat{u}_k &= \sum_{j=0}^{N/2-1} \left[u_{2j} W^{2jk} + u_{2j+1} W^{(2j+1)k} \right] \\ &= \hat{u}_k^e + W^k \hat{u}_k^o \end{aligned} \tag{2.9}$$

This basic split into even and odd coefficients has reduced the operations from $\mathrm{O}(N^2)$ to $\mathrm{O}(N^2/2)$ and this forms the key idea of FFT. The even and odd coefficients in equation 2.9 can be further divided into two more parts further reducing the operations by a factor of 2 and so on till smallest prime number. For example if $\mathrm{N} = 2^M$, then we can repeat this factorizing M times, until transforms of length 1, accounting to only $\log_2 N$ steps (Boyd 2001). This is known as Cooley-Tukey algorithm whose cost of computation is $\mathrm{O}(N \log_2 N)$.

2.1.2 Pseudo-spectral transform methods

The approach taken in the transform method is to use the inverse discrete Fourier transform (DFT) to transform $\hat{u}_m$ and $\hat{v}_m$ to physical space, to perform there a multiplication and then to use the DFT to determine $\hat{w}_k$ (Canuto *et al.* 1988; Boyd 2001).

$$U_j = \sum_{k=-N/2}^{N/2-1} \hat{u}_k e^{-\imath k x_j}; \qquad V_j = \sum_{k=-N/2}^{N/2-1} \hat{v}_k e^{-\imath k x_j} \qquad j = 0, 1, ..., N-1 \tag{2.10}$$

and define

$$W_j = U_j V_j \qquad j = 0, 1, ..., N-1 \tag{2.11}$$

$$\hat{W}_k = \frac{1}{N} \sum_{j=0}^{N-1} W_j e^{\imath k x_j} \qquad k = -N/2, ..., N/2 - 1. \tag{2.12}$$

Using discrete orthogonality relation, it can be shown that

$$\hat{W}_k = \sum_{m+n=k} \hat{u}_m \hat{v}_n + \sum_{m+n=k\pm N} \hat{u}_m \hat{v}_n. \tag{2.13}$$

The second term on the right-hand side is the aliasing error. This error is because of the corruption due to high wave numbers. For example consider $U_j = \sin(2x_j)$ and $V_j = \sin(3x_j)$ with N = 8. The Fourier coefficients are

$$\begin{array}{lcccccccccc} k & = [& -4 & -3 & -2 & -1 & 0 & 1 & 2 & 3 &] \\ \hat{u} & = [& 0 & 0 & \imath & 0 & 0 & 0 & -\imath & 0 &] \\ \hat{v} & = [& 0 & \imath & 0 & 0 & 0 & 0 & 0 & -\imath &] \end{array}$$

The above sequence gives the Fourier coefficients $\hat{u}$, $\hat{v}$ corresponding to wave numbers k. Note that, for $U_j = \sin(2x_j)$, the wave number corresponding to k = ±2 is non-zero and $V_j = \sin(3x_j)$, the wave number corresponding to k = ±3 is non-zero. The Fourier transform of $W_j = U_j V_j = \sin(2x_j)\sin(3x_j) = 0.5(\cos(x_j) + \cos(5x_j))$, leads to coefficients

$$\begin{array}{lcccccccccc} k & = [& -4 & -3 & -2 & -1 & 0 & 1 & 2 & 3 &] \\ \hat{W} & = [& 0 & -0.5 & 0 & 0.5 & 0 & 0.5 & 0 & -0.5 &] \end{array}$$

Here the coefficients corresponding to the wave numbers k = ±3 are due to the aliasing error. The high wave numbers, here k = ± 5, introduced due to the non-linear term W_j, corrupts the low wavenumber, k = ±3 = ±5 ∓ 8, which is the spurious term in equation 2.13. The Fourier coefficients corresponding to the non-linear term W_j should have been

$$\begin{array}{lcccccccccccccc} k & = [& -6 & -5 & -4 & -3 & -2 & -1 & 0 & 1 & 2 & 3 & 4 & 5 &] \\ \hat{W} & = [& 0 & -0.5 & 0 & 0 & 0 & 0.5 & 0 & 0.5 & 0 & 0 & 0 & -0.5 &] \end{array}$$

The higher wave numbers, here k = ± 5, are aliased onto the smaller wave numbers because of the insufficient grid resolution. This is shown in the figure 2.1. If the convolution sums are evaluated as described above, then the method is not true spectral Galerkin method. Orszag (Orszag 1971) termed it a *pseudospectral* (PS) method. The convolution sum in the PS method is evaluated at the cost of 3 FFTs and N multiplications. The total operation count is $(15/2)Nlog_2N$ multiplications. The generalization of the PS evaluation of convolution sums to more than one dimension is straight forward. The use of transform methods enables the evaluation in $O(Nlog_2N)$ operations and the three-dimensional generalization in $O(N^3log_2N)$ operations. This technique was developed independently by Orszag (1969, 1970) and Eliasen, Machenhauer and Rasmussen (1970). It was the single most important development which made spectral Galerkin methods practical for large scale computations (Canuto *et al.* 1988).

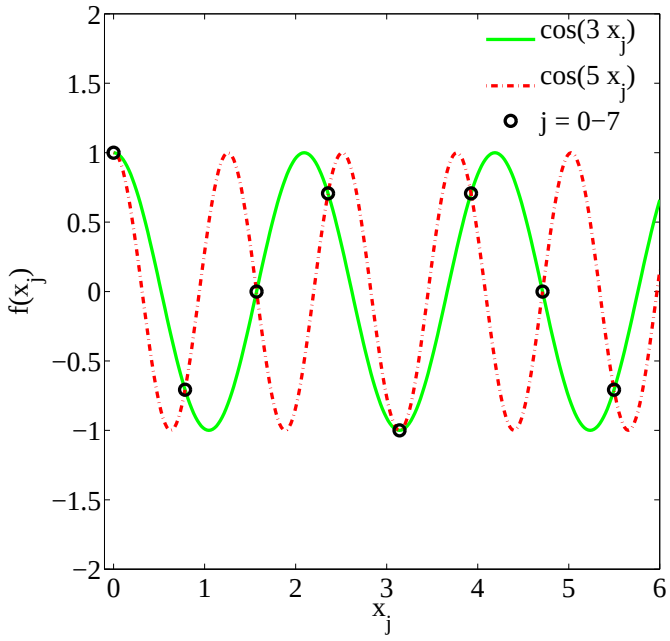

Figure 2.1: Aliasing errors due to high wave numbers corrupting the lower ones. The same set of values at discrete points, represents both the functions $\cos(5x_j)$ and $\cos(3x_j)$.

2.1.3 De-aliasing

The aliasing error is removed by "padding" or "truncation" technique. This technique employs a discrete transform with M points rather than N points, where $M \geq 3N/2$

$$U_j = \sum_{k=-M/2}^{M/2-1} \hat{u}_k e^{-\imath k x_j} \; ; \qquad V_j = \sum_{k=-M/2}^{M/2-1} \hat{v}_k e^{-\imath k x_j} \qquad j = 0, 1, ..., M-1. \tag{2.14}$$

Here $\hat{u}_k$ is same as described in the above section for $k = -N/2, ..., N/2 - 1$ and zero for the rest. Thus the additional wave numbers are padded with zeros.

$$W_j = U_j V_j \qquad j = 0, 1, ..., M-1 \tag{2.15}$$

$$\hat{W}_k = \frac{1}{M} \sum_{j=0}^{N-1} W_j e^{\imath k x_j} \qquad k = -N/2, ..., N/2 - 1. \tag{2.16}$$

Use of discrete transform orthogonality relation (equation 2.3) leads to

$$\hat{W}_k = \sum_{m+n=k} \hat{u}_m \hat{v}_n + \sum_{m+n=k\pm M} \hat{u}_m \hat{v}_n. \tag{2.17}$$

We are only interested in $\hat{W}_k$ for $|k| \leq N/2$, and choose M such that the second term on the right-hand side vanishes for these k. Thus, $M \geq 3N/2$. When this de-aliasing technique is

applied to the example discussed in the previous sub-section, padding gives

$$\begin{array}{rl} k & = [\ -6\ \ -5\ \ -4\ \ -3\ \ -2\ \ -1\ \ 0\ \ 1\ \ 2\ \ 3\ \ 4\ \ 5\ ] \\ \hat{u} & = [\ 0\ \ 0\ \ 0\ \ 0\ \ \imath\ \ 0\ \ 0\ \ 0\ \ -\imath\ \ 0\ \ 0\ \ 0\ ] \\ \hat{v} & = [\ 0\ \ 0\ \ 0\ \ \imath\ \ 0\ \ 0\ \ 0\ \ 0\ \ 0\ \ -\imath\ \ 0\ \ 0\ ] \end{array}$$

Inverse transforming these coefficients, calculating the product in real space and then transforming back to Fourier space we get

$$\begin{array}{rl} k & = [\ -6\ \ -5\ \ -4\ \ -3\ \ -2\ \ -1\ \ 0\ \ 1\ \ 2\ \ 3\ \ 4\ \ 5\ ] \\ \hat{W} & = [\ 0\ \ -0.5\ \ 0\ \ 0\ \ 0\ \ 0.5\ \ 0\ \ 0.5\ \ 0\ \ 0\ \ 0\ \ -0.5\ ] \end{array}$$

Basically, all the possible higher wave numbers which are responsible for aliasing are resolved. Here, the coefficients of higher wave numbers introduced for padding are neglected giving

$$\begin{array}{rl} k & = [\ -4\ \ -3\ \ -2\ \ -1\ \ 0\ \ 1\ \ 2\ \ 3\ ] \\ \hat{W} & = [\ 0\ \ 0\ \ 0\ \ 0.5\ \ 0\ \ 0.5\ \ 0\ \ 0\ ] \end{array}$$

These final set of Fourier coefficients are free of aliasing errors, where the coefficients corresponding to wave numbers, k = ±3, which had spurious errors is zero now. The operation count for this transform method is $(45/4)Nlog_2(3/2N)$, which is roughly 50% larger than the simpler, but aliased method. This technique is sometimes referred to as 3/2-rule. Interpreting the same rule other way round, considering the actual size as 2N/3 rather than N, we get $M \geq N$, which is known as 2/3-rule. In 2/3-rule we work with an array of size N in which we retain only 2/3 of the Fourier coefficients padding the rest.

2.2 Software details

2.2.1 FFTW3

FFTW (Fastest Fourier Transform in the West) is a well established C subroutine library for computing the discrete Fourier transform (DFT) in one or more dimensions, of arbitrary input size, and of both real and complex data (as well as of even/odd data, i.e. the discrete cosine/sine transforms or DCT/DST) (Frigo & Johnson 2013). We used FFTW 3.3.2 version for all the pseudo-spectral results reported. The current version of FFTW incorporates many good ideas from the past thirty years of FFT literature (Frigo & Johnson 2012). FFTW uses the Cooley-Tukey algorithm, the prime factor algorithm, Rader's algorithm for prime sizes, and a split-radix algorithm (with a variation due to Dan Bernstein). FFTW does not use a fixed algorithm for computing the transform, but instead it adapts the DFT algorithm to details of the underlying hardware in order to maximize performance (Frigo & Johnson 2005). Once a FFT algorithm is chosen in order to achieve best performance for a given size N, FFTW uses a high-precision timer to measure the cost of different code choices. Hence, the computation of the transform is split into two phases. First, FFTW's planner learns the fastest way to compute the transform on the machine. The planner produces a data structure called a plan that contains this information

```
/* create plan for r2c DFT */
plan = fftw_mpi_plan_dft_r2c_3d(nx, ny, nz, &rin[0], rout, MPI_COMM_WORLD,
    FFTW_MEASURE);

iplan = fftw_mpi_plan_dft_c2r_3d(nx, ny, nz, rout, &rin[0], MPI_COMM_WORLD,
    FFTW_MEASURE);
```

The 'plan' created above is for DFT of a real three dimensional array 'rin' of size nx×ny×nz to a complex array 'rout'. 'iplan' is for the inverse DFT of complex array 'rout' into a real array 'rin'. Subsequently, the plan is executed to transform the array of input data as dictated by the plan. The plan can be reused as many times as needed by calling execute function

```
/* compute transforms as many times as desired */
fftw_execute(plan) ;
....
fftw_execute(iplan) ;
```

In typical high-performance applications, many transforms of the same size are computed and, consequently, a relatively expensive initialization of this sort is acceptable, like '$FFTW\_MEASURE$'. On the other hand, if you need a single transform of a given size, the one-time cost of the planner becomes significant. For this case, FFTW provides fast planners based on heuristics or on previously computed plans. FFTW supports transforms of data with arbitrary length, rank, multiplicity, and a general memory layout.

Once the variable is transformed to from real to Fourier space, by executing a plan, it has to be normalized accordingly depending on the total size (here oneByNxyz = 1.0/(nx×ny×nz)) of the array as

```
for (i = 0; i < local_n0; i++){
  for (j = 0; j < ny; j++){
    for (k = 0; k < nzh; k++){
      rin(i,j,k,0) *= oneByNxyz ;
      rin(i,j,k,1) *= oneByNxyz ;
      }}}
```

The inverse transform of this normalized Fourier coefficients gives back the original array.

The function $fftw\_mpi\_local\_size\_2d$ is called to find out what portion of the array resides on each processor, and how much space to allocate. Here, the portion of the array on each process is a $local\_n0 \times ny \times (nz/2+1)$ slice of the total array, starting at index $local\_0\_start$. The total number of $fftw\_complex$ numbers to allocate is given by the *alloc_local* return value.

```
alloc_local = fftw_mpi_local_size_3d(nx, ny, nz/2+1, MPI_COMM_WORLD, &local_n0,
    &local_0_start);
```

2.2.2 Panini library

Panini is an in-house generic parallel array class built on advanced generic programming methodologies like Template Meta programming, operator overloading and lazy evaluation of expression (Sah & Ansumali 2012). It allows a user to work with high-level physical abstractions for scientific computation. The distinguishing feature of the meta programming used in this library with that of object oriented programming model used in softwares such as MATLAB is, the concept of 'lazy evaluation', which avoids the use of temporary arrays. It can be efficiently parallelized for large scale scientific coding. Via operator overloading in C++, it has high performance numerical libraries where abstract mathematical notations can be used. The operations are small array sizes is made efficient using Loop Unrolling. This framework can be conveniently used along with the FFTW3 library to make the coding effort minimal.

This framework uses two array templates based vectTiny and vectET based on the array size. For small size arrays (<400 doubles), where the user knows the size in advance, 'vectTiny' class can be used. The syntax for creating an array of doubles of size 3 is

```
vectTiny <double, 3> a = 3.0 ; // double vector of size 3
vectTiny <double, 3> b ; b = 1.0, 2.0, 3.0 ;
vectTiny <double, 3> c ; c = b ;
```

In these declarations, 'double' can be replaced by other datatypes as well. All the elements of array: 'a' are initialized to 3.0, 'b' are initialized to 1.0, 2.0, 3.0 respectively and 'c' is initialized same as the elements of 'b'. It can support math operations like

```
b = sin(a) ;
c = a + b ;
c = 0.5*c + a*b ;
```

For larger arrays whose size is usually dynamically allocated, 'vectET' should be used

```
vectET<double> a(500) ;
vectET< vectTiny <int, 3> > b(400) ;
```

The first statement creates an array 'a' of 500 doubles while the second statement creates an array 'b' of 400 vectTinys (of 3 integers) i.e we have an array 'b' with 3 integers at each of 400 points. vectET variables can also handle basic math operations like addition, scalar multiplication etc.

In this library, *grid3D* is a class to generate three dimensional grid conveniently, hiding the implementation details, using vectTiny and vectET. For example the below codelet creates a three dimensional grid of size ($local\_n0$)×ny×(nz+2).

```
grid3D rin(local_n0, ny, nz+2);
```

Here elements of 'rin' can be accessed by using 'rin(i,j,k)', where i, j and k are the coordinates of the point on the grid.

real-to-complex transforms

The below sample code gives a gist of using Panini with FFTW3 to calculate the derivative of a 3D- scalar field, in a parallel environment using MPI.

```
alloc_local = fftw_mpi_local_size_3d(nx, ny, nz/2+1, MPI_COMM_WORLD, &local_n0,
    &local_0_start);
grid3D rin(local_n0, ny, nz+2);
rout = (fftw_complex *) &rin[0] ;

/* create plan for in-place r2c DFT */
plan  = fftw_mpi_plan_dft_r2c_3d(nx, ny, nz, &rin[0], rout, MPI_COMM_WORLD,
    FFTW_MEASURE);
iplan = fftw_mpi_plan_dft_c2r_3d(nx, ny, nz, rout, &rin[0], MPI_COMM_WORLD,
    FFTW_MEASURE);

/* initializing rin to some function */
for (i = 0; i < local_n0; i++)
  for (j = 0; j < ny; j++)
    for (k = 0; k < nz; k++){
      double z = 2.0*M_PI*k /(double)(nz) ;
      double x = 2.0*M_PI*(i+local_0_start) /(double)(nx) ;
      double y = 2.0*M_PI*j /(double)(ny) ;

      rin(i,j,k) = cos(x)*cos(y)*sin(z);
      }

/* compute transforms as many times as desired */
fftw_execute(plan);

for (i = 0; i < local_n0; i++){
  for (j = 0; j < ny; j++){
    for (k = 0; k < nzh; k++){
      rin(i,j,k,0)*= oneByNxyz ;
      rin(i,j,k,1)*= oneByNxyz ;
      }}}

vectET<double> kd(nx, 0.0);
/* Wave number k - note the sequence */
for ( i = 0; i < nx/2 ; i++) kd[i] = i ;

for ( i = nx/2; i < nx; i++) kd[i] = i - nx ;

double temp ;
for (i = 0; i < local_n0; i++){
  for (j = 0; j < ny; j++){
    for (k = 0; k < nzh; k++){
      temp = rin(i,j,k,0);
```

```
        rin(i,j,k,0) = -kd[k]* rin(i,j,k,1);
        rin(i,j,k,1) = kd[k]*temp ;
        }}}

fftw_execute(iplan);
```

FFTW uses a slice decomposition meaning that the 3D domain is decomposed along one of the axes, here it is X-direction. It uses the real-to-complex transform in FFTW to transform a real data from real to Fourier space. In-place transform is employed here minimizing the memory usage, where the real array and the complex array are stored in the same array, hence using the Hermitian symmetry of the complex data due to a real transform. Note that the brackets '()' are overloaded, which are used for both real and complex data, where the real data has three inputs corresponding to the three coordinates and the complex data has four inputs, the fourth input being either zero or one corresponding to the real and imaginary part. The complex variable (rout) is pointed to the starting address of the real variable (rin) so as to achieve an in-place transform and the real array address is type casted to complex so as match the pointers. Array 'kd' gives the wave numbers which shows the sequence in which Fourier coefficients are arranged in FFTW. Finally partial derivative w.r.t z of the 3D field (rin) is computed and then transformed back to real space.

real-to-real transforms

The Fourier transform of a real-even function f(-x) = f(x) is real-even. For a real-odd function f(-x) = -f(x), $\imath$ times the Fourier transform is real-odd. Similar results hold for a discrete Fourier transform, and thus for these symmetries the need for complex inputs/outputs is entirely eliminated. Moreover, one gains a factor of two in speed/space from the fact that the data are real, and an additional factor of two from the even/odd symmetry: only the non-redundant (first) half of the array need be stored. The result is the real-even DFT (REDFT) and the real-odd DFT (RODFT), also known as the discrete cosine and sine transforms (DCT and DST), respectively.

Because of the discrete sampling, the data is even/odd around a sampling point or around a point half way between two data points. This gives rise to several invariants in transforms, depending on the sampling points at both ends. We use for n real numbers (from j = 0...n-1)

- FFTW_REDFT10 (DCT-II, "the DCT"): even around j = -0.5 and even around j = n-0.5
- FFTW_REDFT01 (DCT-III, "the IDCT"): even around j = 0 and odd around j = n
- FFTW_RODFT10 (DST-II): odd around j = -0.5 and odd around j = n-0.5
- FFTW_RODFT01 (DST-III): odd around j = -1 and even around j = n-1

A size-4 REDFT10 (DCT-II) of the data abcd corresponds to the size-8 logical DFT of the even array abcddcba, shifted by half a sample. The inverse of of REDFT10/ RODFT10 is REDFT01/ RODFT01 and vice versa.

```
alloc_local = fftw_mpi_local_size_3d(nxBy2, nyBy2, nzBy2, MPI_COMM_WORLD,
    &local_n0, &local_0_start) ;
gridFlow3D u(local_n0, nyBy2, nzBy2);

plan_u  = fftw_mpi_plan_r2r_3d(nxBy2, nyBy2, nzBy2, u, u, MPI_COMM_WORLD,
    FFTW_RODFT10, FFTW_REDFT10, FFTW_REDFT10, FFTW_MEASURE);
iplan_u = fftw_mpi_plan_r2r_3d(nxBy2, nyBy2, nzBy2, u, u, MPI_COMM_WORLD,
    FFTW_RODFT01, FFTW_REDFT01, FFTW_REDFT01, FFTW_MEASURE);

fftw_execute(plan_u) ;
rightShift_comm ( lnx, taskid, numtasks, nyBy2, nzBy2, u ) ;

for ( i = 0; i < nxBy2 ; i++ ) kd[i] = i ;

leftShift_comm ( lnx, taskid, numtasks, nyBy2, nzBy2, u ) ;
fftw_execute(iplan_u) ;
```

The above sample code shows the forward and inverse transform of a 3D real scalar field 'u', odd in X-direction and even in Y and Z-directions. The array 'kd' gives the sequence of wave numbers in which the Fourier coefficients are given by FFTW. It should be noted that in an odd transform the wave numbers start from k = 1 rather than k = 0. The function 'rightShift_comm' shifts the elements of the array 'u' in X-direction by 1 unit, so that wave numbers in all the directions start from k = 0, and the new column created is filled with zeros. This shift is important, as we deal with different arrays, even/odd symmetric in different directions and perform operations on them, like finding vorticity, considering that the wave numbers in all three directions start from k = 0 (else basic operation like adding arrays with different symmetries in different directions becomes cumbersome in Fourier space). Care should be taken that while performing an inverse transform of an odd field, it should be shifted back by 1 unit, so that the wave number starts from k = 1 in the odd direction. The function 'leftShift_comm' shifts back the array making it suitable for an inverse transform using FFTW.

2.3 Third order Runge-Kutta scheme

In the current work, we are interested in the time evolution of the ODE of the form

$$\frac{dU}{dt} = F[t, U(t)] \tag{2.18}$$

For this purpose, we use Runge-Kutta (RK) three-stage third order scheme (3,3), which requires only two levels of storage(2N-storage, where N is the dimension of the system of ODEs) by Williamson (1980).. This scheme requires evaluation of intermediate quantities.

$$\begin{aligned} k_1 &= F\left(t_n + c_1 h, U_n\right), \\ k_2 &= F\left(t_n + c_2 h, U_n + h a_{2,1} k_1\right), \\ k_3 &= F\left(t_n + c_3 h, U_n + h(a_{3,1} k_1 + a_{3,2} k_2)\right), \end{aligned} \tag{2.19}$$

where h is the time step considered, and c1, c2, c3, $a_{2,1}$, $a_{3,1}$, $a_{3,2}$ are given in table 2.1 . In terms of these quantities, the 3-stage algorithm is

$$\begin{aligned} dU_j &= A_j dU_{j-1} + hF(U_j) \qquad A_1 = 0, \\ U_j &= U_{j-1} + B_j dU_j \qquad j = 1, 2, 3, \end{aligned} \tag{2.20}$$

In this method, only dU and U are to be stored at each stage resulting in a 2N storage. In terms of Butcher table the scalar coefficients are (Carpenter & Kennedy 1994)

$$\begin{array}{c|cc} c_1 & & \\ c_2 & a_{2,1} & \\ c_3 & a_{3,1} & a_{3,2} \\ \hline & b_1 & b_2 \quad b_3 \end{array} = \begin{array}{c|cc} 0 & & \\ \frac{1}{3} & \frac{1}{3} & \\ \frac{3}{4} & -\frac{3}{16} & \frac{15}{16} \\ \hline & \frac{1}{6} & \frac{3}{10} \quad \frac{8}{15} \end{array} \Longrightarrow \begin{array}{c|c} A_1 & B_1 \\ A_2 & B_2 \\ A_3 & B_3 \end{array} = \begin{array}{c|c} 0 & \frac{1}{3} \\ -\frac{5}{9} & \frac{15}{16} \\ \frac{153}{128} & \frac{8}{15} \end{array}$$

Table 2.1: (3,3) RK 2N-storage scheme coefficients

2.3.1 Navier-Stokes in Fourier domain

The PS method solves the three-dimensional Navier-Stokes (NS) equations in periodic domains. In terms of the Fourier coefficients $\tilde{u}_j(\mathbf{k})$, j labeling the spatial dimensions, the NS equations read as follows:

$$\partial_t \tilde{u}_j(k_l) = -\nu\, k^2 \tilde{u}_j - \left(\delta_{ij} - \frac{k_i\, k_j}{k^2}\right) F_i(k_l), \tag{2.21}$$

where $F(\mathbf{k})$ is the Fourier coefficient of the non-linear advection term and the pressure term is eliminated via the projection operator

$$\mathcal{P}\phi = \left(\delta_{ij} - \frac{k_i\, k_j}{k^2}\right) \phi, \tag{2.22}$$

which projects the NS equations onto the incompressible manifold (Frisch 1995).

Most applications of spectral methods to partial differential equations the spatial discretization is spectral but the temporal discretization uses conventional Taylor series based methods. The stability restriction arising from the convection terms can be more severe than the viscous stability limit. Third order low-storage Runge-Kutta time-differencing scheme for the nonlinear term and an integrating-factor technique on diffusion term are employed. In problems with periodic boundary conditions the preferred technique for handling constant-coefficient linear terms is exact integration. This integrating-factor technique has found extensive use in Fourier Galerkin simulations of homogeneous turbulence. In this method, the viscous term is most conveniently handled via analytical integration (Rogallo 1981), to deliver:

$$\partial_t \left[\tilde{u}_j(k_l)\, \exp\left(\nu\, k^2\, t\right)\right] = -\exp\left(\nu\, k^2\, t\right) \left(\delta_{ij} - \frac{k_i\, k_j}{k^2}\right) F_i(k_l). \tag{2.23}$$

This equation can be solved numerically by any convenient time-integration scheme. The treatment of the linear term is both unconditionally stable and exact. The accuracy and stability

restrictions of the method arise solely from the non-linear term.

As a time-integration scheme for equation 2.23, we chose a low-storage version of the Runge-Kutta third order scheme 2.19, which requires only two levels of storage(Williamson 1980).

2.4 Summary

In this work, a parallel MPI PS solver based on Panini and FFTW is developed. We have chosen the "2/3" rule, due to its simplicity and ease of parallel implementation. For the MPI (Message Passing Interface) implementation of parallel Fourier transform, we have used FFTW library (version 3), which provides a comprehensive collection of fast C routines for computing the Discrete Fourier Transform (DFT) (Frigo & Johnson 2005). The initial conditions being highly symmetric in space, only odd ($FFTW\_RODFT10/FFTW\_RODFT01$) and even ($FFTW\_REDFT10FFTW\_REDFT10$) transforms (as described in previous section) are used, thus reducing the problem size to one eighth (half in each direction) (Kida 1985), as compared to the full original domain. The non-linear term requires eight Fourier transforms in our code. We evaluate three inverse Fourier transforms to obtain the velocity components in real space, and five forward transforms to evaluate non-linear terms.

Chapter 3

Universal mechanism for saturation of vorticity growth

3.1 Introduction

Turbulent flow is a chaotic, nonlinear multi-scale phenomenon which we come across in every-day life. Flow of air over automobiles and aircrafts, smoke from a cigarette, cumulus clouds, atmospheric and oceanic currents are a few examples of turbulent flows. It can be defined as that state of matter characterized by a loss of coherence in space and time, as a result of the non-linear interaction of a large number of degrees of freedom, in excess of billions even for most familiar phenomena, such as flow past an automobile (Frisch 1995; Chen *et al.* 2003; Davidson 2004). For many real life flow applications, fluids are incompressible and their dynamics is governed by Navier-Stokes(NS) equations

$$\begin{aligned} \partial_t u_\alpha + u_\beta \partial_\beta u_\alpha + \frac{1}{\rho}\partial_\alpha p = \frac{1}{Re}\nabla^2 u_\alpha, \\ \partial_\beta u_\beta = 0 \end{aligned} \tag{3.1}$$

where u_i is velocity, ρ is fluid density, p is pressure and Re is Reynolds number ($= UL/\nu$ where U is characteristic velocity, L is the characteristic length and ν is the kinematic viscosity of the fluid). The incompressibility, a non-local constraint, manifests itself as the pressure Poisson equation, obtained by taking the divergence of NS equations

$$\nabla \cdot NS \Longrightarrow \frac{1}{\rho}\nabla^2 p = \partial_\alpha \partial_\beta u_\alpha u_\beta \tag{3.2}$$

Though the governing equations are well known for centuries, turbulence is one of the important unsolved problems of classical physics. Apart from non-locality, another difficulty in solving NS is the non-linearity of the advection term $F_i = u_j \partial_j u_i$ which in terms of its Fourier coefficients is

$$\hat{F_\alpha}(k_\gamma) = \sum_{k_\gamma^m + k_\gamma^n = k_\gamma} \imath \mathrm{k}_\beta \hat{u}_\beta(k_\gamma^m)\hat{u}_\alpha(k_\gamma^n) \tag{3.3}$$

where $\hat{u}_\alpha(k_\gamma)$ is the Fourier transform of velocity. It can be clearly seen that $\hat{F_\alpha}(k_\gamma)$ is not only comprised of the scale $\mathbf{k}$, but is a convolution sum of velocity over different scales. This mixing or interaction of scales leads to enormous degrees of freedom as the Reynolds number increases.

In a direct numerical simulation (DNS), all the length scales till the Kolmogorov length scale η, which scales as $Re^{-3/4}$, is resolved. If the largest length scale in the flow is given by l_0 then the degrees of freedom required in one dimension is $l_0/\eta \sim \mathrm{Re}^{3/4}$. Therefore resolution required in three dimensions for a DNS is $N \sim \mathrm{Re}^{9/4}$. Therefore the computational resources required

even for simple turbulent flows, whose Reynolds number is usually of the order of 10^6, are quite high. This raises a formidable computational barrier even for the most powerful computational methods in the foreseeable future, let alone analytical methods. Thus, often the goal of large scale DNS is to provide insight into phenomenology of turbulence and its origin.

Recent advances in computational hardware allows for long time integration with relatively large number of degrees of freedom feasible. In the present work, using large scale computations, we investigate and report universal features in the transient dynamics towards steady state turbulence. This is a comparatively less studied aspect of turbulence, perhaps due to the fact that universal behavior is usually associated to time-asymptotic states, whereas transient features, being driven by morphological details, are typically regarded as inherently non-universal.

The present simulations of transient decaying three-dimensional flows suggest that the saturation of vorticity growth takes place through the onset of transient, and yet universal structures. The first is the appearance of universal $k^{-3}\log k$ spectrum in the transient towards the Kolmogorov's statistical steady-state, while the second is a concurrent outburst of enstrophy, which is carried by high-stretch and high-vorticity transient structures. Although rare and short-lived, such structures are sufficiently strong and long-lived to signal the transit of the system through a universal $k^{-3}\log k$ state, on its way towards the asymptotic Kolmogorov spectrum. Part of this work is published in Thantanapally *et al.* (2013).

This chapter is organized as follows: Section 3.2 discusses the scaling laws in energy spectrum and Onsager's criticism on Kolmogorov's theory. In section 3.3, we review the main arguments behind vorticity dynamics and blow-up issues. In section 3.4, details of various initial conditions used in present work is provided. Section 3.5 discuss the energy scaling laws in the transient and it is argued that initial transient is inviscid. Statistical analysis of the numerical results is also presented in this section. Finally, a brief conclusion is presented in section 3.7 after which details of the movies supporting the claims made in this work is given.

3.2 Energy cascade and power laws

The idea of describing a flow in terms of eddies was proposed by Lewis Fry Richardson (Richardson & Chapman 1965). He suggested that a flow can be described in terms of eddies of different sizes. The larger eddies gain kinetic energy from the mean flow and breaks-down to smaller eddies by stretching and instabilities. These smaller eddies in turn breakdown to even smaller eddies (as shown in figure 3.1 (Frisch 1995)) and so on till small enough size, where viscous forces dominate and energy is dissipated. This transfer of kinetic energy from larger to smaller scales is termed as energy cascade.

This theory was later adopted by A. N. Kolmogorov to give a quantitative assessment using dimensional arguments. He argued that the time required for an eddy of size l and rms velocity fluctuation u_l, to transfer energy to smaller scales is $\tau_l \sim l/u_l$, whereas time required for the same eddy to dissipate its energy using viscosity is $\tau_l^{viscous} \sim l^2/\nu$. Depending on the dominance among the above two time scales, three different range of scales can be identified namely injective range, inertial range and dissipative range. He assumed that the statistics of the small scales are isotropic and universal for all turbulent flows at high enough Reynolds number and that there is no dissipation of energy in the breaking of eddies to smaller eddies. Therefore there is

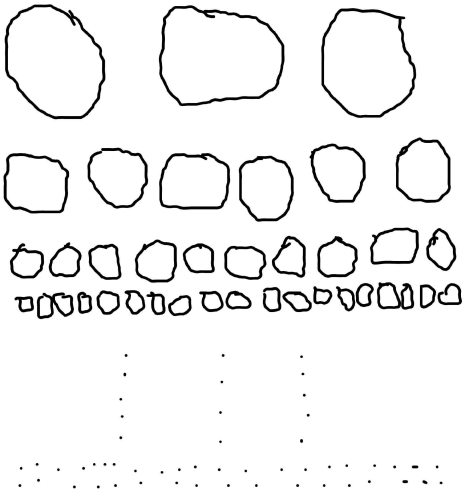

Figure 3.1: Picture of energy cascade showing the breakdown of larger eddies to smaller eddies in a turbulent flow

a hierarchy of scales created $L >> r >> \eta$ where L is large scale anisotropic eddies injecting energy, r is the universal isotropic eddies just transferring energy (because of the dominance of inertial forces over viscous forces, hence called as inertial range) to smaller ones in their range and η is the scale where dissipation actually takes place.

In the inertial range energy transfer rate $\Pi(r)$ should be

$$\Pi(r) \sim \frac{E(r)}{\tau_r} \sim \frac{u_r^2}{r/u_r} \tag{3.4}$$

At statistical steady state, this transfer rate should be balanced with energy dissipation (ϵ) at smaller scales. Thus, the velocities and time scales in the inertial range is universally determined only by ϵ and r in that range

$$u_r \sim \epsilon^{1/3} r^{1/3}, \qquad \tau_r \sim \epsilon^{-1/3} r^{2/3} \tag{3.5}$$

The scale η, also known as the Kolmogorov scale is identified as the scale beyond which viscous forces dominate, thus at this scale dissipative and transfer times are equal, which imply that the Reynolds number based on Kolmogorov scales is unity

$$\frac{\eta u_\eta}{\nu} = 1 \tag{3.6}$$

Using equation 3.5 and equation 3.6, Kolmogorov length scale is

$$\eta \sim \epsilon^{-1/4} \nu^{3/4}. \tag{3.7}$$

In the inertial subrange the kinetic energy spectrum E(k) as a function of wavenumber k has a universal form uniquely determined by ϵ and k, independent of ν giving

$$E(k) = C\epsilon^{2/3} k^{-5/3} \tag{3.8}$$

where C is a universal Kolmogorov constant. This energy scaling in inertial range is qualitatively shown in the figure 3.2. The same result can also be arrived from the similarity and scale invariance arguments in the inertial range, which gives the four-fifths law in real space using the third order structure function. In the limit of infinite Re number, the third order (longitudinal) structure function of homogeneous isotropic turbulence, evaluated for increments l small compared to integral scale, is given in terms of mean energy dissipation per unit mass ϵ by (Frisch 1995)

$$\langle(\delta v_{||}(\mathbf{r},\mathbf{l}))^3\rangle = -\frac{4}{5}\epsilon l \tag{3.9}$$

This scaling in energy spectrum is validated both computationally and experimentally.

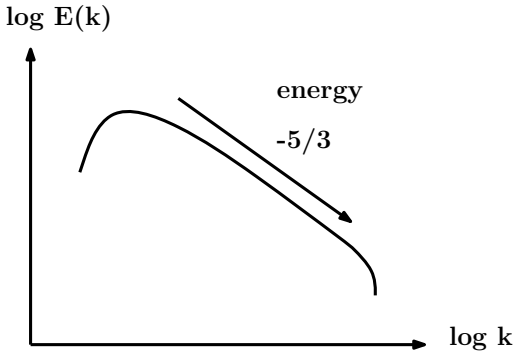

Figure 3.2: Energy spectrum in 3D turbulence

Another important result using similar dimensional analysis is, in 2D turbulence, put forth by Kraichnan(Kraichnan 1967). The main difference between 2D and 3D turbulence is that the vortex stretching term is zero in the former. This difference results in the conservation of both energy and enstrophy at high enough Reynolds number (vanishing viscosity) which results in an inverse energy cascade (energy being transferred from smaller to larger wave numbers) with a slope of -5/3

$$E(k) = C\epsilon^{2/3}k^{-5/3}. \tag{3.10}$$

and a direct cascade of enstrophy (from larger to smaller wave numbers) with a slope of -3 in the energy spectrum

$$E(k) = C'\epsilon_w^{2/3}k^{-3}, \tag{3.11}$$

ϵ_w being the enstrophy flux.

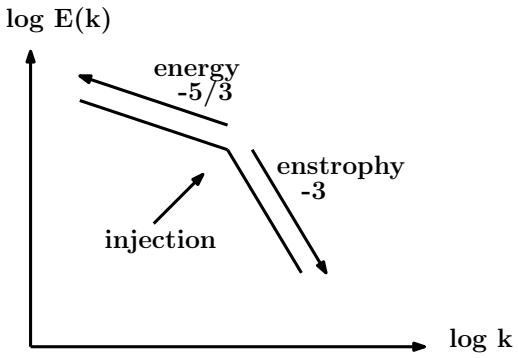

Figure 3.3: Energy spectrum in 2D turbulence

This scaling in the energy is qualitatively shown in figure 3.3, where the energy is pumped at an injection wavenumber and we see a inverse cascade of energy towards smaller wave numbers scaling as -5/3 and a forward cascade of enstrophy towards larger wave numbers scaling as -3.

3.2.1 Onsager's criticism

Onsager was one of the first to comment on possible ramifications of existence of power law in energy spectrum as predicted by Kolmogorov's hypothesis (Eyink & Sreenivasan 2006). His argument was that Kolmogorov length-scale goes to zero as $\mathrm{Re} \to \infty$ because

$$\eta \sim l_0 \mathrm{Re}^{-3/4}. \tag{3.12}$$

On the other hand, the total time T^* for energy introduced at the scale l_0 to cascade down to scale η is given by

$$T^* = \sum_i t_i = A \sum_i l_i^{2/3}, \tag{3.13}$$

which is the sum of an infinite convergent geometric series for $\mathrm{Re} \to \infty$. Thus, it takes a finite time for energy to cascade to infinitesimal scales.

Furthermore, from mean energy balance, the mean energy dissipation is

$$\epsilon \equiv -\frac{dE}{dt} = 2\,\nu\Omega, \tag{3.14}$$

where Ω is the average enstrophy in the domain. This equation suggests that for $\mathrm{Re} \to \infty$, energy dissipation rate ϵ is finite only when $\Omega \to \infty$ (Frisch 1995). The above argument only gives a flavor of the singularity argument but there is no rigorous proof for the existence of singularity in Navier-Stokes equations from smooth initial conditions. This chapter attempts to comment on the existence of singularity and try to find the universal features, if any, in the transient dynamics finally leading to statistical steady state of Kolmogorov scaling in energy spectrum.

3.3 Vorticity dynamics and blow-up

The evolution of a fluid flow is often analyzed in terms of the vorticity field, $\vec{\omega} = \vec{\nabla} \times \vec{u}$, $\vec{u}$ being the flow velocity. The time evolution for which is

$$\begin{aligned} \frac{D\omega_\alpha}{Dt} &= \omega_\beta \partial_\beta u_\alpha + \nu \Delta \partial_\beta \partial_\beta \omega_\alpha \\ \frac{D}{Dt} &= \frac{\partial}{\partial t} + u_\beta \partial_\beta \end{aligned} \tag{3.15}$$

where D/Dt is the material derivative. The term $\omega_\beta \partial_\beta u_\alpha$ has two effects, tilting and stretching, on the vortex tube. This can be seen in the coordinate system aligned with the vorticity direction of a vortex tube as

$$\omega_\beta \partial_\beta u_\alpha = \underbrace{\omega_z \frac{\partial u}{\partial z}\mathbf{i} + \omega_z \frac{\partial v}{\partial z}\mathbf{j}}_{\text{tilting}} + \underbrace{\omega_z \frac{\partial w}{\partial z}\mathbf{k}}_{\text{stretching}} \tag{3.16}$$

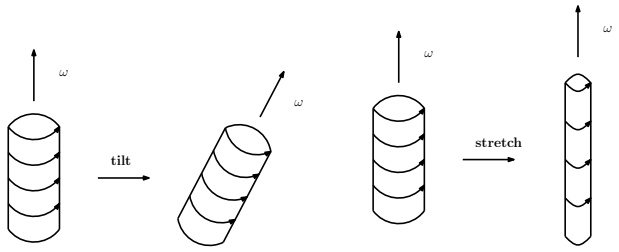

Figure 3.4: Depiction of tilting and stretching of a vortex tube

As shown in figure 3.4, second term in equation tilt-stretch is the stretching component which stretches the tube along the vorticity axis thereby increasing/decreasing the vorticity in that direction and the other component (tilting) just tilts the vortex tube giving rise to a vorticity component perpendicular to the initial vorticity direction.

The dynamics of vorticity can be conveniently analyzed in terms of local enstrophy $\Omega = \vec{\omega} \cdot \vec{\omega}/2$. The evolution equation for local enstrophy is

$$\frac{D\Omega}{Dt} = 2s\Omega + \nu\omega_\alpha \partial_\beta \partial_\beta \omega_\alpha, \qquad s = \frac{\omega_\beta \partial_\beta u_\alpha \omega_\alpha}{\omega^2}, \tag{3.17}$$

where s is the vortex stretching term, namely the growth(decay) rate of the local enstrophy. Hereafter, in the rest of the text we refer s as stretching. This representation elicits the two basic contributions to the vorticity growth (decay), as it is carried along by the fluid, namely a viscous dissipative sink, and the stretching term, which vanishes in two dimensions, since vorticity is then perpendicular to the plane of motion. Vast amount of literature discussing the dynamics of enstrophy including interplay between its production and dissipation is available(Tsinober *et al.* 1997; Holm & Kerr 2002; Donzis *et al.* 2008).

Initial transient dynamics of the flow is expected to be fairly inviscid in which dissipation can be neglected and viscosity plays a leading role only in the late stage of the evolution. If the norm of the strain tensor $S_{\alpha\beta} \equiv (\partial_\alpha u_\beta + \partial_\beta u_\alpha)/2$ is loosely identified with the vorticity magnitude $|\omega_\alpha|$, times a proportionality factor λ, the equation 3.17 takes the form

$$d\Omega/dt = \lambda \Omega^{3/2}. \tag{3.18}$$

Such an argument of approximating S_{ij} is indeed loose, because the vorticity and strain tensors carry a fairly different physical content, rotation versus deformation, respectively. Nevertheless, for $\lambda = \text{Const} > 0$, this scalar equation exhibits a finite-time singular solution,

$$\Omega(t) = \Omega_0 \left(\frac{t - t_c}{t_0 - t_c} \right)^{-2} \tag{3.19}$$

at $t_c = t_0 + 2/(\lambda\sqrt{\Omega_0})$, due to the coherent drive of the vortex stretching term (Frisch *et al.* 2003). This picture of blow up in enstrophy is qualitatively plotted in figure 3.5 Geometrically,

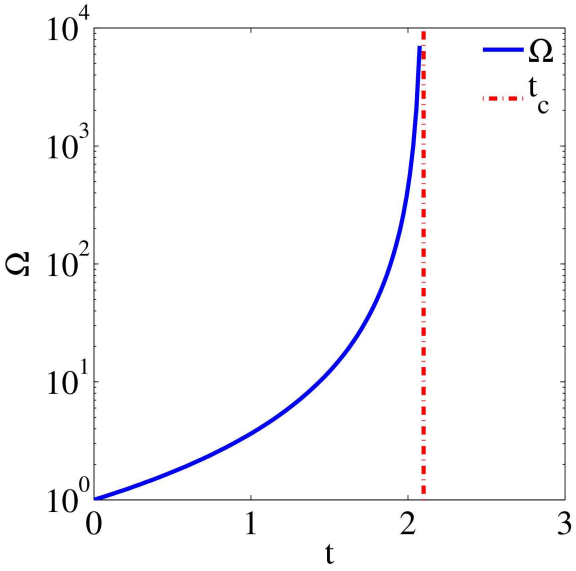

Figure 3.5: Qualitative picture of blow-up in enstrophy at $t_c \sim 2.1$

this corresponds to a vortex tube getting increasingly thinner and more intense, until its core annihilates, thus leading to a singular blow-up. Vast amount of work on finite-time singularities, starting from symmetric initial conditions, is available in the literature, (Pelz 2001; Cichowlas & Brachet 2005; Grafke *et al.* 2008; Hou & Li 2008; Bustamante & Brachet 2012). Several counter blow-up arguments have also been raised, which usually appeal to more detailed insights into the dynamic morphology of turbulence (Frisch *et al.* 2003). Notable among them is the so-called non-linear depletion mechanism, which proposes that vorticity tubes would naturally self-tame their growth, upon bending and eventually collapsing into locally two-dimensional-like structures, which automatically annihilate the non-linear stretching term.

Despite their heuristic appeal, none of the above arguments has managed to gain the status of a rigorous proof, or theorem, whence the scope for extensive numerical simulations. To date, these have brought up the following picture: The smooth initial configuration develops a fast-growing enstrophy stage, driven by a positive average vortex stretching term. The stretched configurations then undergo a number of sudden morphological events, such as vortex break-up and mergers. Even though such simulations and analytical studies are typically performed on inviscid (Euler) flows, one can reasonably expect that such fast-growing transient would remain virtually inviscid also in high Reynolds number simulations. In the long term for NS simulations, such low dimensional structures, evolve into a tangle of vortices, supporting the $k^{-5/3}$ Kolmogorov spectrum, eventually inclusive of slight anomalous corrections, due to intermittent bursts. In line with these expectations, the present analysis is based on high-Reynolds number Navier-Stokes simulations with smooth initial conditions described in the following section.

3.4 Initial Conditions

This section briefly describes the set of initial conditions for decaying flows used in present work. Three sets of initial conditions, namely Kida-Pelz, Taylor-Green and Hill's vortices, are analyzed

in detail, to show the scaling in the energy spectrum to be discussed in the subsequent sections. All of these initial conditions represent flows dominated by vortex stretching. The vorticity equation is invariant under the space translations, the space rotations and plane reflections. Therefore if the velocity field has a symmetry at an initial instant which is invariant under these transformations of variables, it will never be lost in the course of evolution (Kida 1985). The first is the Kida flow, which is most symmetric and the next initial condition is the Taylor-Green vortex, which is slightly less symmetric than the former. In this work we simulate only one-eigth of the total domain i.e half in each direction, therefore using only mirror symmetries. Finally, a set of Hill's vortices is considered, for which no symmetry is assumed. This order was followed to rule out effects of special symmetries of the flow on the universal features described in this work.

3.4.1 Kida-Pelz flow

Kida proposed a class of highly-symmetric periodic initial conditions, for the computational study of high Reynolds number flows known as Kida-Pelz (KP) initial condition (Kida 1985):

$$\begin{aligned} u_x\,(x,\,y,\,z) &= U_0\,\sin\,x\,(\cos\,3y\,\cos\,z - \cos\,y\,\cos\,3z),\\ u_y\,(x,\,y,\,z) &= U_0\,\sin\,y\,(\cos\,3z\,\cos\,x - \cos\,z\,\cos\,3x),\\ u_z\,(x,\,y,\,z) &= U_0\,\sin\,z\,(\cos\,3x\,\cos\,y - \cos\,x\,\cos\,3y). \end{aligned} \tag{3.20}$$

The mirror symmetries and rotational symmetries in this initial condition are compactly given by

$$u_x(x,y,z) = u_y(z,x,y) = u_z(y,z,x), \tag{3.21}$$

$$\begin{aligned} u_x(x,y,z) &= -u_x(2\pi - x, y, z),\\ &= u_x(x, 2\pi - y, z),\\ &= u_x(x, y, 2\pi - z). \end{aligned} \tag{3.22}$$

$$\begin{aligned} u_x(x,y,z) &= -u_x(\pi - x, z, y),\\ &= u_x(x, \pi - z, y). \end{aligned} \tag{3.23}$$

These symmetries expressed in terms of Fourier coefficients is

$$\hat{u}_x(k_1,k_2,k_3) = \begin{cases} \hat{u}_y(k_3,k_1,k_2) = \hat{u}_z(k_2,k_3,k_1)\\ -\hat{u}_x(-k_1,k_2,k_3) = \hat{u}_x(k_1,-k_2,k_3) = \hat{u}_x(k_1,k_2,-k_3)\\ \pm\hat{u}_x(k_1,k_3,k_2) \quad \text{for } k_1,k_2,k_3 = \text{even/odd}\\ 0 \qquad \text{otherwise} \end{cases} \tag{3.24}$$

Thus, the information of a single component of the velocity in a fundamental box ($0 \leq$ x, y, z $\leq \pi/2$) which is 1/64 in volume of the periodic box, with only $N^3/192$ independent degrees of freedom out of a total $3N^3$ is sufficient to describe the whole velocity field. This initial condition is shown by the iso-surfaces of vorticity magnitude in figure 3.6. This reduces both memory and computational requirements considerably, making this an attractive initial condition for the DNS

of turbulence. Also, it has been argued by Kerr (1993) that more symmetries than the ones present in Taylor-Green vortex are preferred in order to observe a singularity. Thus, KP flow is thought to be a more likely candidate for finite time singularity than the TG flow Cichowlas & Brachet (2005). Thus, this flow was used as a potential initial condition by many, such as Pelz (2003); Gulak & Pelz (2005), to study the problem of Euler blow-up. DNS of viscous turbulence was analyzed, using this initial flow condition by Boratav & Pelz (1994). Spectral methods are used in Kida & Murakami (1997); Boratav & Pelz (1994, 1995, 1997) for the numerical investigations starting with these initial conditions. Recent articles on the turbulence analysis of symmetric flows in a periodic box include Orlandi & Pirozzoli (2010); Orlandi *et al.* (2012).

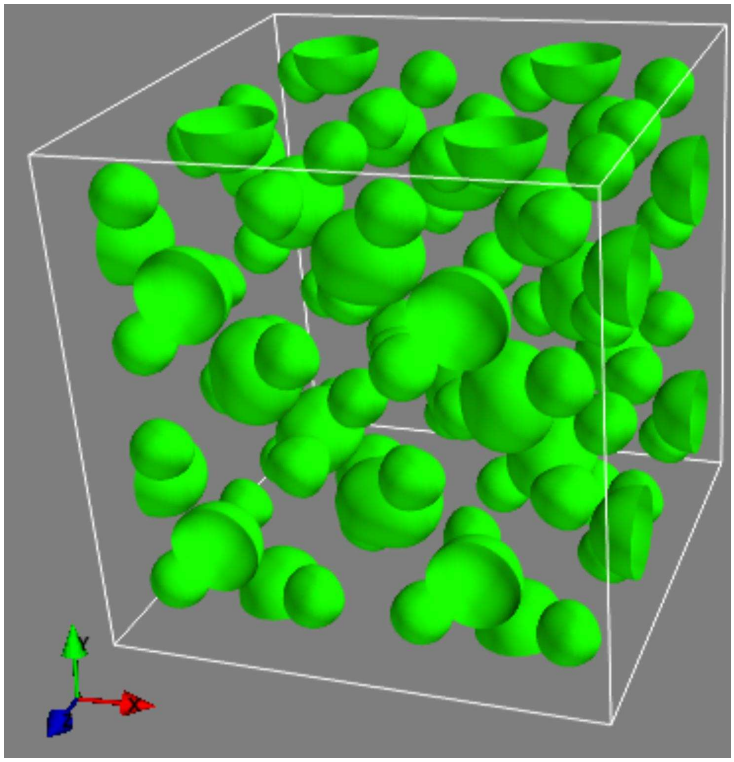

Figure 3.6: Iso-surfaces of vorticity magnitude for KP initial condition

3.4.2 Taylor-Green

The Taylor-Green (TG) flow is one of the simplest setup to investigate the generation of small scales by three-dimensional vortex stretching and the resulting onset of turbulence Brachet *et al.* (1983). The TG initial condition is

$$\begin{aligned} u_x(x,\,y,\,z) &= U_0 \sin x \cos y \cos z, \\ u_y(x,\,y,\,z) &= -U_0 \cos x \sin y \cos z, \\ u_z(x,\,y,\,z) &= 0. \end{aligned} \tag{3.25}$$

The mirror symmetries symmetries in this initial condition are

$$\begin{aligned} u_x(x,y,z) &= -u_x(2\pi - x, y, z), \\ u_y(x,y,z) &= u_y(2\pi - x, y, z), \\ u_x(x,y,z) &= u_x(x, 2\pi - y, z), \\ u_y(x,y,z) &= -u_y(x, 2\pi - y, z), \\ u_x(x,y,z) &= u_x(x, y, 2\pi - z), \\ u_y(x,y,z) &= u_y(x, y, 2\pi - z). \end{aligned} \tag{3.26}$$

and the rotational symmetries are

$$\begin{aligned} u_x(x,y,z) &= u_x(2\pi - x, y, z), \\ u_y(x,y,z) &= -u_y(2\pi - x, y, z). \end{aligned} \tag{3.27}$$

The symmetries in this initial condition are shown by plotting iso-surfaces of vorticity in figure 3.7. Thus for a three dimensional system rather than $3N^3$ independent degrees of freedom, only $N^3/64$ are required, thus reducing the memory requirements by factor of 64. The dynamics of both the inviscid and viscous TG three-dimensional vortex flows have been investigated extensively in the literature.

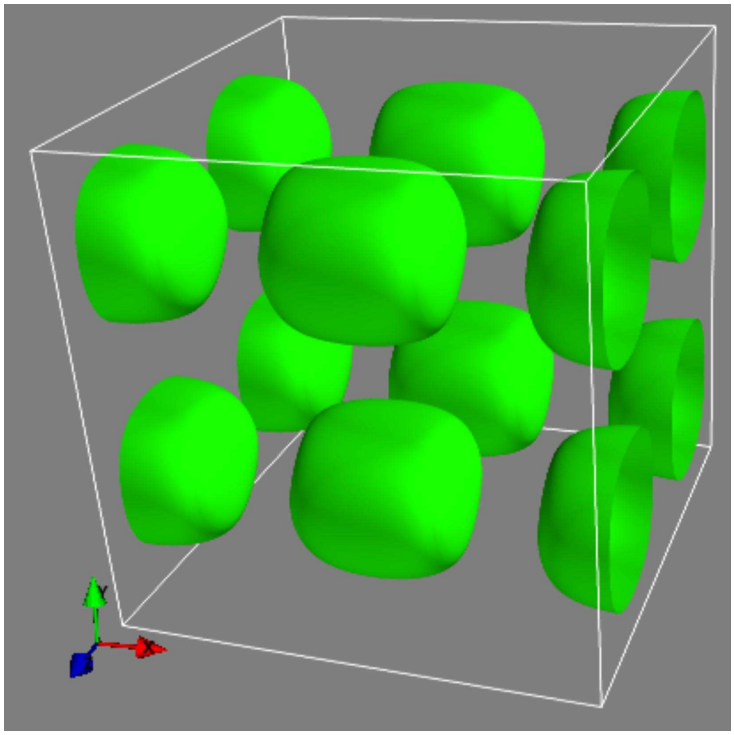

Figure 3.7: Iso-surfaces of vorticity in Taylor-Green initial condition

3.4.3 Hill's spherical vortex

The third initial condition investigated in this work is the Hill's spherical vortex (Aivazis & Pullin 2001). Each vortex consists of a vorticity-containing sphere, in which the vortex lines are

circles about the direction of propagation and the magnitude of the vorticity is proportional to the radius of the circle. Six Hill's vortex blobs, moving perpendicular to each side of the periodic cube, towards the center, have been used as an initial condition to trigger turbulence, as shown in figure 3.8, as a result of their collisions at the center. In cylindrical polar coordinate system (R, ϕ, z), if a vortex of radius a moves with speed U along the z-axis, and the location of its center is Z, then the vorticity distribution, $\omega = (0, \omega_\phi, 0)$ is (Aivazis & Pullin 2001)

$$\omega_\phi = \begin{cases} AR & \text{if } R^2 + (z-Z)^2 < a^2 \\ 0 & \text{if } R^2 + (z-Z)^2 > a^2 \end{cases} \tag{3.28}$$

where A = 15 U/2 a^2. In terms of velocity field it is approximately

$$u_R = \begin{cases} 3UR\frac{(z-Z)}{2a^2} & \text{if } r <= a \\ 3a^3UR\frac{(z-Z)}{2r^5} & \text{if } r >= a \end{cases}$$

$$u_z = \begin{cases} U\frac{5a^2-3(z-Z)^2-6R^2}{2a^2} & \text{if } r <= a \\ a^3U\frac{3(z-Z)^2-r^2}{2r^5} & \text{if } r >= a \end{cases} \tag{3.29}$$

where $r^2 = R^2 + (z-Z)^2$, $R = r\sin\theta$, $z - Z = R\cos\theta$ such that the component of $\mathbf{r}$ along the direction of advancement is $r\cos\theta$. Although the Hill's vortex is not represented exactly by the velocity field, (as signaled by a non-zero compressibility), due the jump in vorticity across their surface, the simulation remains nearly incompressible ($|\nabla \cdot \mathbf{u}| \leq 10^{-3}$).

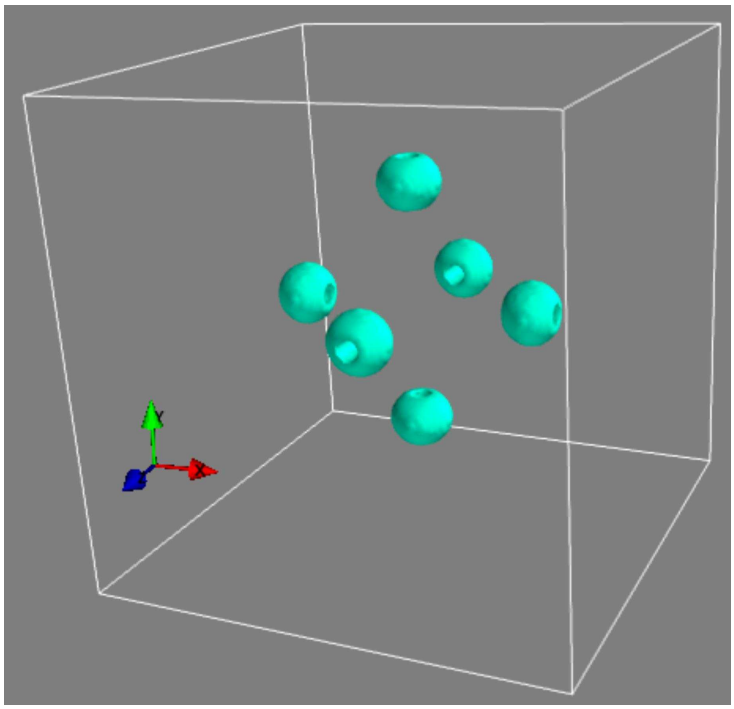

Figure 3.8: Vorticity iso-surfaces of Hill's spherical vortices moving perpendicular to the sides of the cube towards the center at t = 0.

3.5 Energy spectrum and universality

In this section, we focus our attention on the transient towards steady state, and in particular, on the time interval around the primary peak in maximum vorticity. Maximum vorticity ω_{max} at a given time is

$$\omega_{max}(t) = \|\omega(x_\alpha, t)\|_\infty \tag{3.30}$$

which is same as finding the vorticity magnitude with highest value in the entire domain at a given point of time, as shown in figure 3.9 for KP flow. In particular, we investigate the time

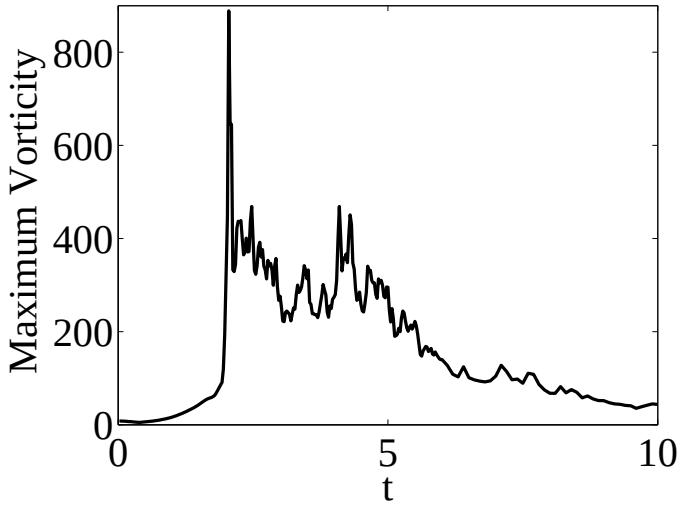

Figure 3.9: Maximum vorticity ω_{max} for KP at Re = 5000 with 1024^3 resolution.

evolution of kinetic energy spectrum E(k). Our simulations suggest that the spectrum observed in connection with local enstrophy saturation, around t $\sim$ 2 (for KP), are convincingly close to $k^{-3}\log k$. In order to highlight the generality of our results, figure 3.10, reports a normalized energy spectrum as a function of the dimensionless wavenumber $k\,\eta$ and dimensionless energy $E(k)/E_n$, where $E_n = (\epsilon\,\nu^5)^{1/4}$. This figure highlights the occurrence of $k^{-3}\log k$ spectrum, which suggest a spontaneous arrangement of the flow towards a quasi 2D structure, as an effective mechanism to tame vorticity growth (Frisch 1995). Away from the peak, normalized energy spectrum at later time, when turbulence is well developed, is plotted in figure 3.11 to inspect the attainment of the Kolmogorov 5/3 law. This indicates that our simulations are convincingly in high Re domain.

Figure 3.12, presents an extended sequence of energy spectra (top and mid panels), corresponding to the square symbols in the bottom panel, where the time evolution of the maximum vorticity for the KP flow is shown. This sequence highlights a tendency towards a $k^{-3}\log k$ spectrum in the initial stage of the evolution, up to about $t = 2.5$, and the subsequent long-term rearrangement towards a Kolmogorov spectrum (see also the associated movies in the Supplementary Material). Similar extended sequence of energy spectra is shown for TG simulation in figure 3.13, where peak event is observed around $t \sim 6.5$, around which the energy spectrum aligns towards a $k^{-3}\log k$ scaling.

To further validate the scaling in energy spectrum around the peak in maximum vorticity,

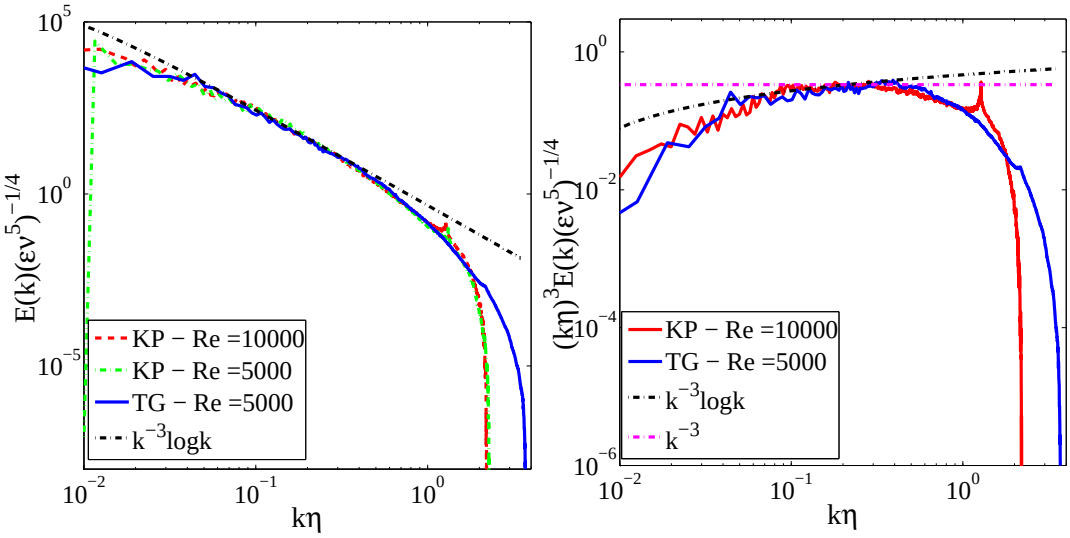

Figure 3.10: (**Left**) Normalized energy spectra of the KP and TG flow, at the t = 2.04 for KP and t = 6.45 for TG. In both cases, the figures provide neat evidence of a $k^{-3}\log k$ spectrum, in correspondence with the vorticity peak. (**Right**) Compensated energy spectra of the KP and TG flows. The figure provides a clear evidence of a $k^{-3}\log k$ spectrum, to be compared with the horizontal k^{-3} line. This highlights a clear need for a logarithmic correction, in synchrony with the first maximum vorticity.

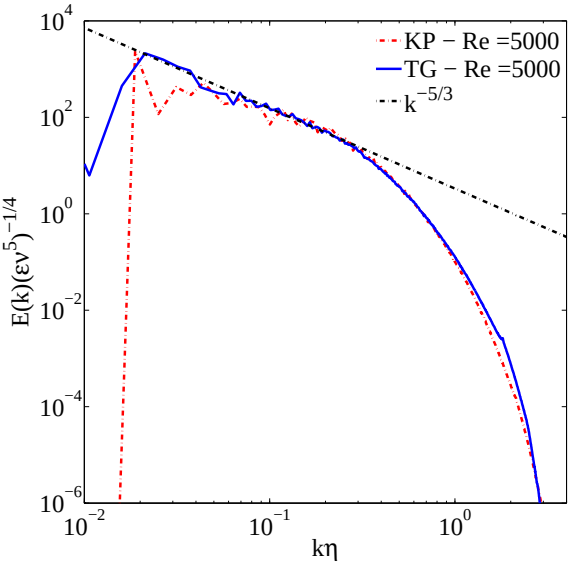

Figure 3.11: Normalized energy spectra of the KP and TG flows, at $t = 10$ and $t = 12$, respectively. In both cases, the figure shows evidence of the $k^{-5/3}$ Kolmogorov scaling.

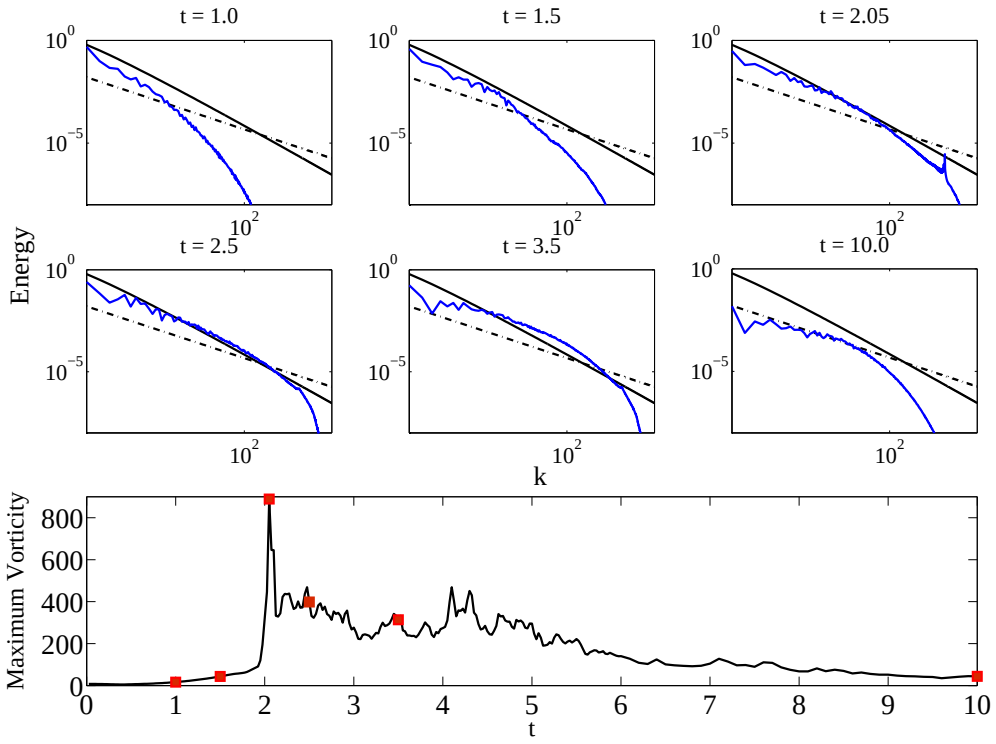

Figure 3.12: Energy spectra at $t = 1, 1.5, 2.05, 2.5, 3.5, 10$ (top and mid panels), corresponding to the square symbols in the bottom panel, reporting the time evolution of the maximum vorticity for the KP flow at Re $= 5000$ with 1024^3 resolution. Continuous and dashed straight lines indicate $k^{-3}\log k$ and $k^{-5/3}$ respectively.

we show an extended sequence of energy spectra in time for a set Hill's vortices initial condition (as discussed in the earlier section) in figure 3.14. This spectra also confirms that the energy scaling has in fact a $k^{-3}\log k$ scaling in sync with the peak in maximum vorticity.

Finally, the spectra tend to adjust towards the long-term $-5/3$ Kolmogorov shape. Inspection of the spectral movies (see Supplementary Material) suggests of this "oscillation" between the $k^{-3}\log k$ and $k^{-5/3}$ power spectra, the residency time in $k^{-3}\log k$ being shorter and shorter as time unfolds. The same qualitative picture is observed for both KP and TG vortices, the latter exhibiting more persistent multiple peaks (at a given Re). This lends further weight to the conjecture that freely decaying, three-dimensional homogeneous, incompressible fluid turbulence, exhibits universality not only in its asymptotic, Kolmogorov, steady-state, but also in the transient stage towards such an asymptotic steady-state. It seems that the long-term Kolmogorov state cannot be attained, unless the system goes first through the $k^{-3}\log k$ transient.

Here, it should be noted that, though figure 3.10 is showing less than half a decade of $k^{-3}\log k$ range, the trend is pretty much towards $k^{-3}\log k$, the relatively narrow range being due to limited numerical power for high Reynolds flows. On the other hand, to extrapolate our results to very high Re domain, Euler simulations are also performed with different resolutions. From Euler simulation results, as plotted in figure 3.15, it is apparent that the trend is towards a $k^{-3}\log k$ spectrum, which is then visible for over a decade. Sensitivity analysis of the spectrum, via plotting $k^3E(k)$ as a function of k in figure 3.15 (left), clearly indicates the requirement for a logarithmic correction. This is indeed confirmed with the curve fit to the simulation data

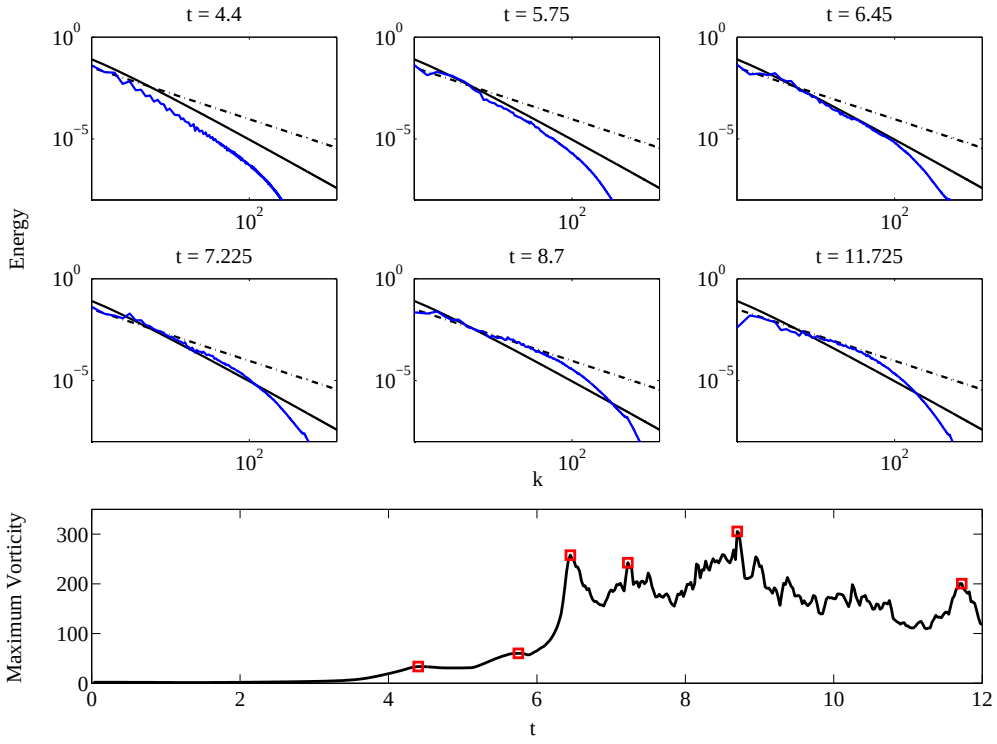

Figure 3.13: Energy spectra at $t = 4.4, 5.75, 6.45, 7.225, 8.7, 11.725$ (top and mid panels), corresponding to the square symbols in the bottom panel, reporting the time evolution of the maximum vorticity for the TG flow at $\mathrm{Re} = 5000$ with 1024^3 resolution. Continuous and dashed straight lines indicate $k^{-3}\log k$ and $k^{-5/3}$ respectively.

yielding, $k_0 = 3.2 \pm 0.6$ and $n = 1.33 \pm 0.09$ as shown in figure 3.15 (right), which is decidedly a better fit to the simulation data than a plain k^{-3} spectrum.

3.5.1 Initial transient: An inviscid growth

In this section it is argued that the transient dynamics, i.e the attainment of $k^{-3}\log k$ in energy spectra, observed in the simulations of the KP and TG flows is inviscid in nature. In figure 3.16, time evolution of energy at different Reynolds number for the case of Kida-Pelz(KP) and Taylor-Green flows is reported, which demonstrates that, in the initial stage of the evolution ($t < 2.5$ and $t < 6.7$ respectively), the system behaves like an almost inviscid fluid. Figure 3.17 presents the total enstrophy, $\Omega(t)$, integrated over the entire volume, as well as the maximum vorticity, $\omega_{max}(t)$, as a function of time, for the KP and TG flows at $\mathrm{Re} = 5000$ with 1024^3 resolution. This figure reveals the existence of a sharp peak in ω_{max} at $t \sim 2.1$ and $t \sim 6.5$ respectively, marking the end of the inviscid exponential enstrophy growth. The primary peak is followed by a series of minor sub-peaks, on top of a slowly decreasing trend towards the statistical steady state.

To show that the peak event in maximum vorticity is taking place in the high Re regime we report the Taylor micro-scale Re for KP and TG in figure 3.18. Reynolds number based on

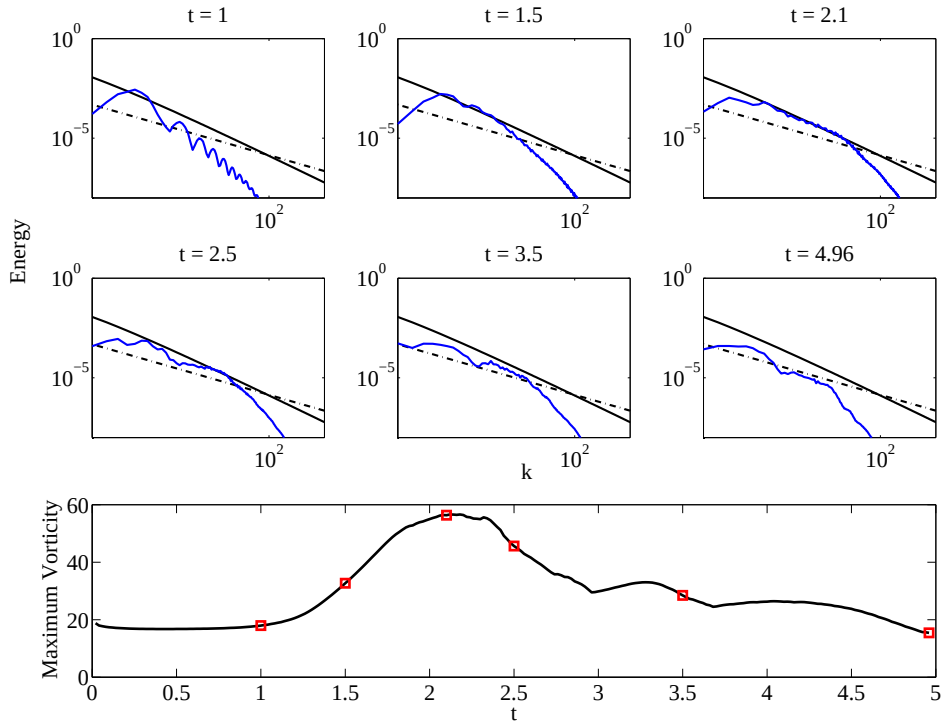

Figure 3.14: Energy spectra at $t = 1.0, 1.5, 2.1, 2.5, 3.5, 4.96$ (top and mid panels), corresponding to the square symbols in the bottom panel, reporting the time evolution of the maximum vorticity for a set of Hill's vortices with 768^3 resolution. Continuous and dashed straight lines indicate $k^{-3}\log k$ and $k^{-5/3}$ respectively.

Taylor micro-scale is (Frisch 1995)

$$Re_\lambda = \sqrt{\frac{10}{3}}\frac{E(t)}{\nu\sqrt{\Omega}}. \tag{3.31}$$

In figure 3.18, Re_λ is plotted as a function of time, for both KP and TG, showing that the Taylor micro-scale Reynolds number is much above hundred around the peak event in both cases. In fact $Re_\lambda \sim 380$ at t = 2.05 for KP flow and $Re_\lambda \sim 327$ at t = 6.45 for TG flow, at Re = 5000 with a resolution of 1024^3.

Since total dissipation is approaching zero rapidly (Table 3.1), while spectra are becoming closer and closer to $k^{-3}\log k$, we believe that vorticity saturation is basically inviscid and even local dissipation has not much role to play in this stage of the evolution. This scenario is verified with additional inviscid (Euler) runs, which indicates inviscid nature of scaling as given in table 3.1. We remind that the minor energy loss in the case of Euler simulations is due to the numerical dissipation. To back-up this assertion, figure 3.19 reports the peak time, t_p, at which the main peak occurs, as a function of the Reynolds numbers. For both KP and TG vortices, this peak time is largely insensitive to the Reynolds number, in the full explored range $1000 < \mathrm{Re} < 10000$ of NS simulations.

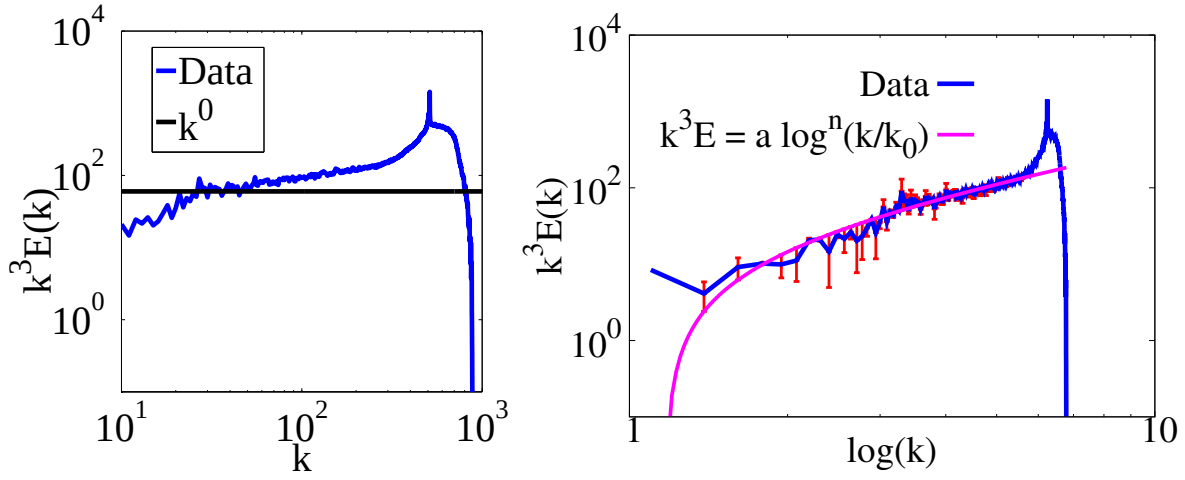

Figure 3.15: Compensated energy spectrum at t = 2.0 for Euler simulations of KP flow, (**left**) showing the necessity for logarithmic correction. (**Right**) Compensated energy spectrum as a function of $\log k$ in order to get the exact form of logarithmic correction. Curve fit of simulation data yielding $k_0 = 3.23149 \pm 0.6298$ and $n = 1.32687 \pm 0.08791$ exposing sensitivity to logarithmic correction.

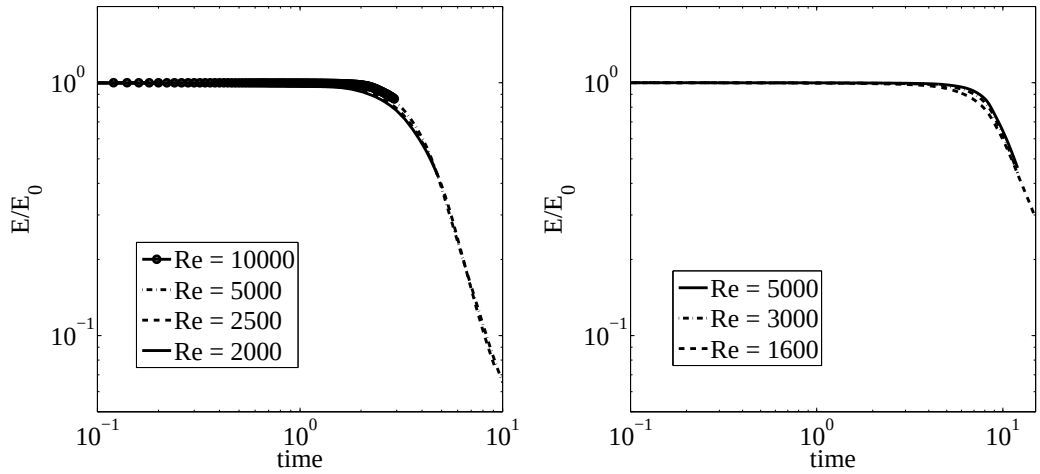

Figure 3.16: Time evolution of the kinetic energy at different Reynolds numbers for KP and TG flows respectively. The figure demonstrates that the kinetic energy is conserved up to within a few percents in the initial stage of the evolution till the peak event ($t < 2.5$ and $t < 6.7$ respectively). Total enstrophy and maximum vorticity of the KP and TG flow respectively at $Re = 5000$ with 1024^3 resolution, as a function of time.

Reynolds number	% of initial energy	Peak time	Resolution
5000	95.924	2.050	1024^3
10000	97.71707	2.040	1536^3
Euler	99.99867	2.025	1024^3
Euler	99.99973	2.025	1536^3

Table 3.1: Total energy dissipation, in correspondence with $k^{-3} \log k$ spectrum, for the case of KP flow

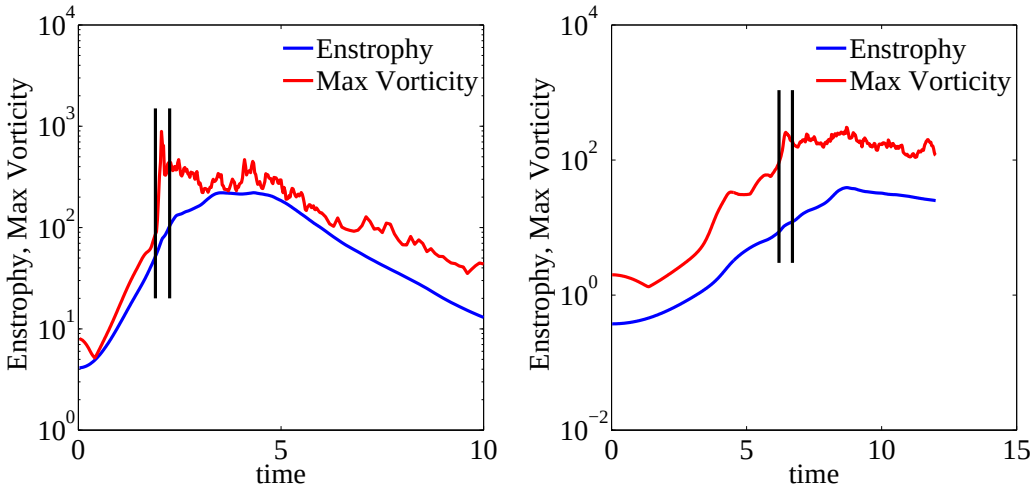

Figure 3.17: Total enstrophy and maximum vorticity of the KP (left) and TG (right) flows at $Re = 5000$ with 1024^3 resolution, as a function of time.

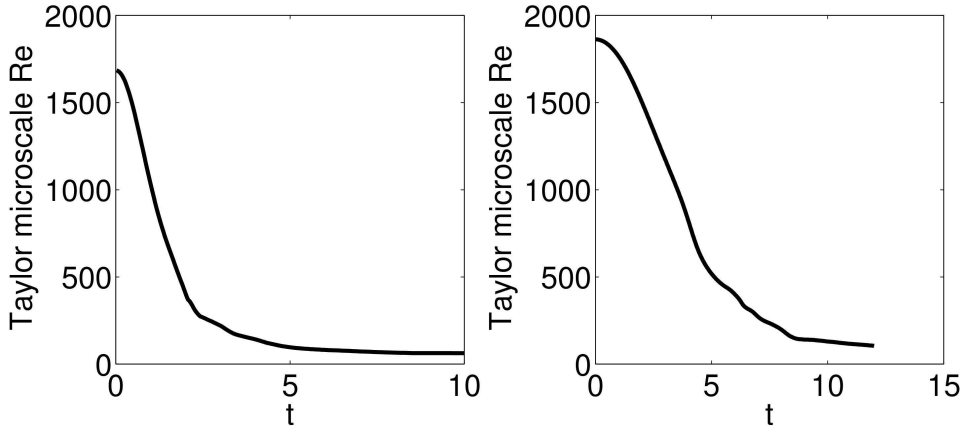

Figure 3.18: Taylor micro-scale Reynolds number Re_λ for KP (left) and TG (right) flows at Re $= 5000$ with 1024^3 resolution.

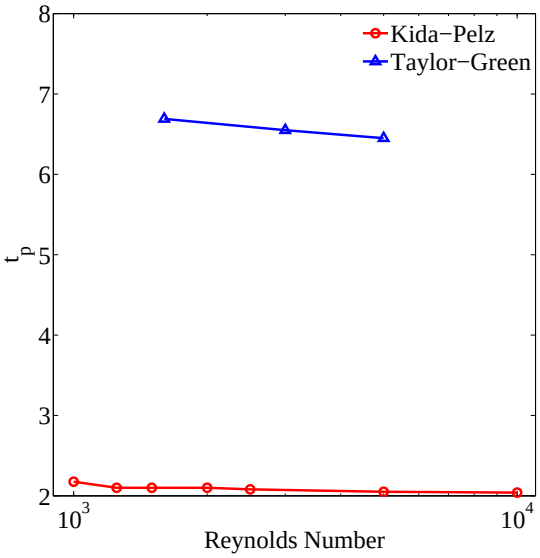

Figure 3.19: Time at which maximum vorticity is attained with Reynolds number for KP and TG initial conditions. The figure shows that this event is almost independent of Re suggesting inviscid dynamics in the flow at that particular instant.

3.5.2 Possible mechanisms to tame the vorticity growth

While existing theories based on non-linear depletion concentrate on topological changes of vortex tubes (Frisch *et al.* 2003), the simulations of this work suggest that blowup may stop due to the interactions between vortex tubes of dissimilar stretching and magnitude. This is illustrated in figure 3.20, where it is shown that each iso-surface of vorticity supports a mix of positive and negative stretch, throughout the domain. Though any conclusive, direct proof of the dominance of such interaction cannot be offered, nevertheless a series of indirect proofs, lending weight to such a conjecture is obtained. The first indirect evidence is the detection of quasi-two-dimensional spectrum, with exponent close to -3 (in fact $k^{-3}\log k$), which suggests that such events would be promoted by an underlying reverse energy cascade (Kraichnan 1967).

For this purpose, we plot the third order structure function given by

$$S_3(r) = \left\langle \left[(v_\beta(x_\alpha + r_\alpha) - v_j(x_\alpha)) \frac{r_\beta}{r} \right]^3 \right\rangle \tag{3.32}$$

where v_β is the velocity, r_α is the position vector from a given point x_α and $\langle\rangle$ denotes spatial average. The figure 3.21 (left) near peak ($t = 2.05$), clearly shows that the third-order structure function $S_3(r)$ is positive at sufficiently large separations, $r > 10$, thereby pointing to an inverse energy cascade at those scales. On the other hand, around the Kolmogorov time-zone($t = 4.8$), $S_3(r)$ is mostly negative, in the small-scale region ($r < 10$), thereby signaling a direct energy cascade.

Spectral exponents between $2.68-3.29$, right after the rms vorticity maximum, were reported before, in spectral simulations of TG vortex at Re $= 1600$ and $Re = 3000$ (Brachet *et al.* 1983; Orlandi & Pirozzoli 2010). However, potential connections between two-dimensionalization of the local fluid structure and taming of enstrophy blow-up, have not received any special attention

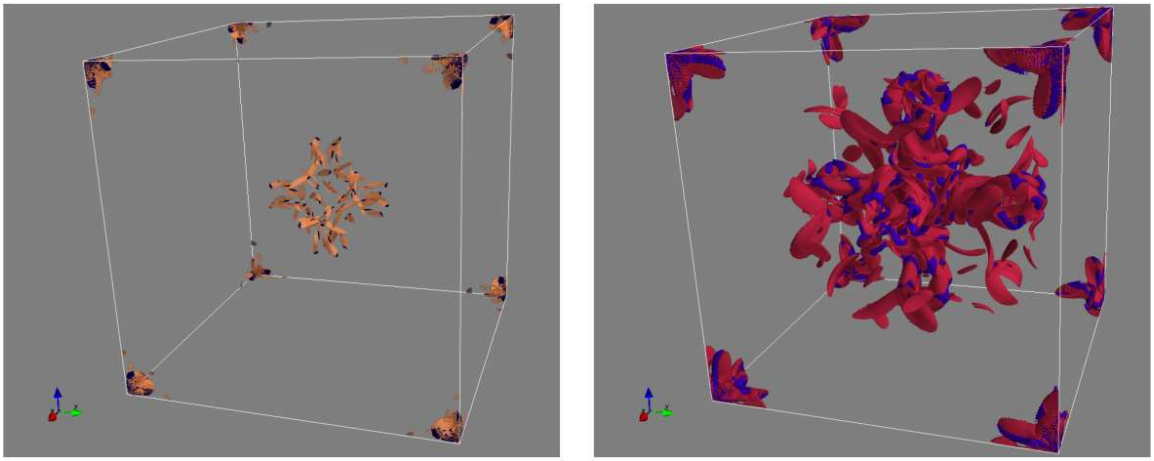

(a) (b)

Figure 3.20: Iso-contours of vorticity in KP flow for $Re = 2000$ with 768^3 resolution at $t = 1.15$. (**a**) High vorticity at $\omega = 58$, with positive (orange) and negative (black) stretching. (**b**) Low vorticity at $\omega = 29$ with positive (red) and negative (blue) stretching. These pictures highlight the coexistence of positive and negative stretch regions within the same iso-surface and shows the dominance of positive stretch structures at this early stage of the evolution.

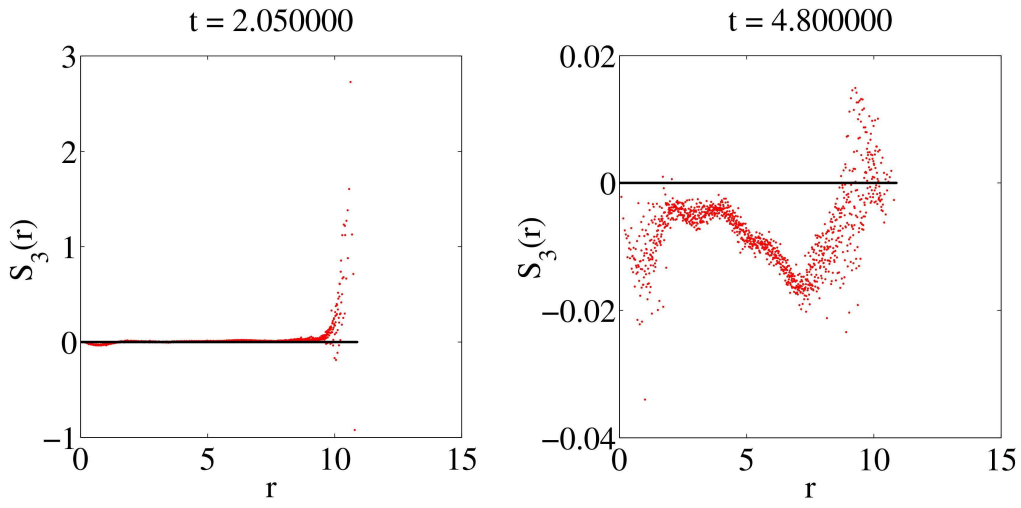

Figure 3.21: Structure function $S_3(r)$ near peak (left) and near the Kolmogorov time region (right) of the KP flow at $Re = 2000$ with 768^3.

to date. The running argument being that transients are relatively uninformative, as they depend on non-universal morphological details, as opposed to the universal statistical features exposed by energy spectra in the time-asymptotic regime. Here, it is contended that even the morphology-driven transient dynamics can exhibit universality. Figure 3.22 shows that ribbon like two-dimensional structures intertwined with each other, as predicted by non-linear depletion mechanism emerges due to non-linear interactions.

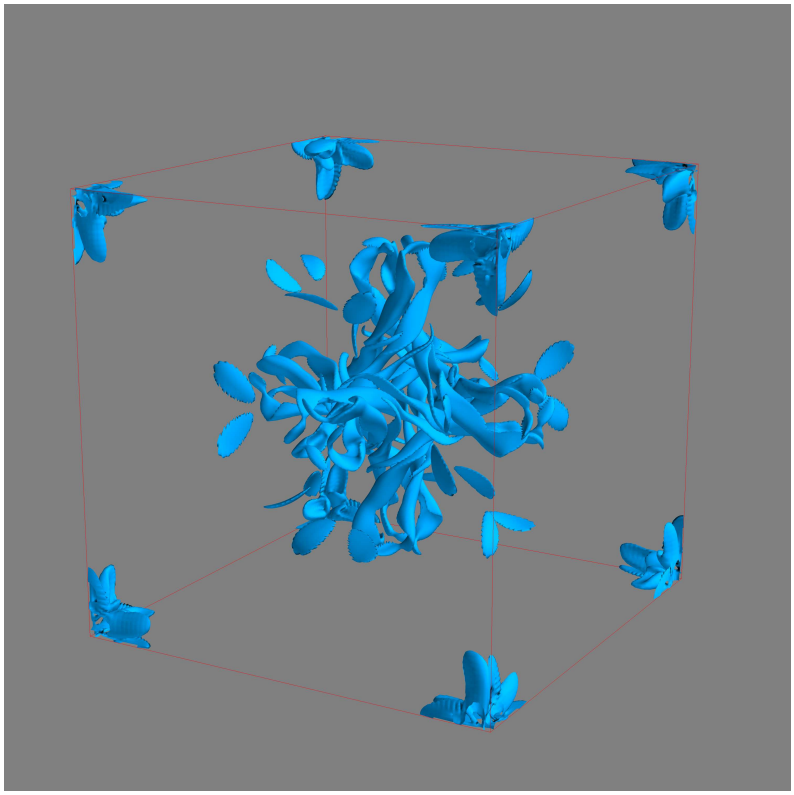

Figure 3.22: KP flow around the peak at Re = 1000 with 512^3 resolution. This figure shows the ribbon/ lasagna like two dimensional structures intertwined with each other, supporting the non-linear depletion.

On the other hand, since the spectra obtained look convincingly closer to $k^{-3}\log k$ than k^{-3}, there is decided scope to pursue a detailed analysis of the transient, especially in the close vicinity of the primary peak. It is reminded that the logarithmic correction bears a major conceptual importance, as it implies that the flow is not just locally smooth, but supports instead non-local effects, leading to quasi-two dimensional physics, namely a significant scale separation between the large-scale straining structures and the small-scale strained ones. Note that the departure from a pure k^{-3} power-law and the associated $\log k$ correction, as well recognizable in figure 3.10, indicates that the flow is marginally non-smooth. This observation is also backed up by the detection of a local inverse energy cascade in coincidence with the universal quasi-two-dimensional transient as shown in figure 3.21.

3.5.3 Statistical analysis

In this section, we describe a statistical analysis of the correlation between the stretch term s, as defined in equation 3.17 and the local enstrophy. For this purpose we define four basic types of structures, namely Low-vorticity-Negative-stretch (LN), High-vorticity-Positive-stretch (HP), Low-vorticity-Positive-stretch (LP), High-vorticity-Negative-stretch (HN) as shown in the figure 3.23, based on low (high) vorticity and positive (negative) stretch are introduced. In the

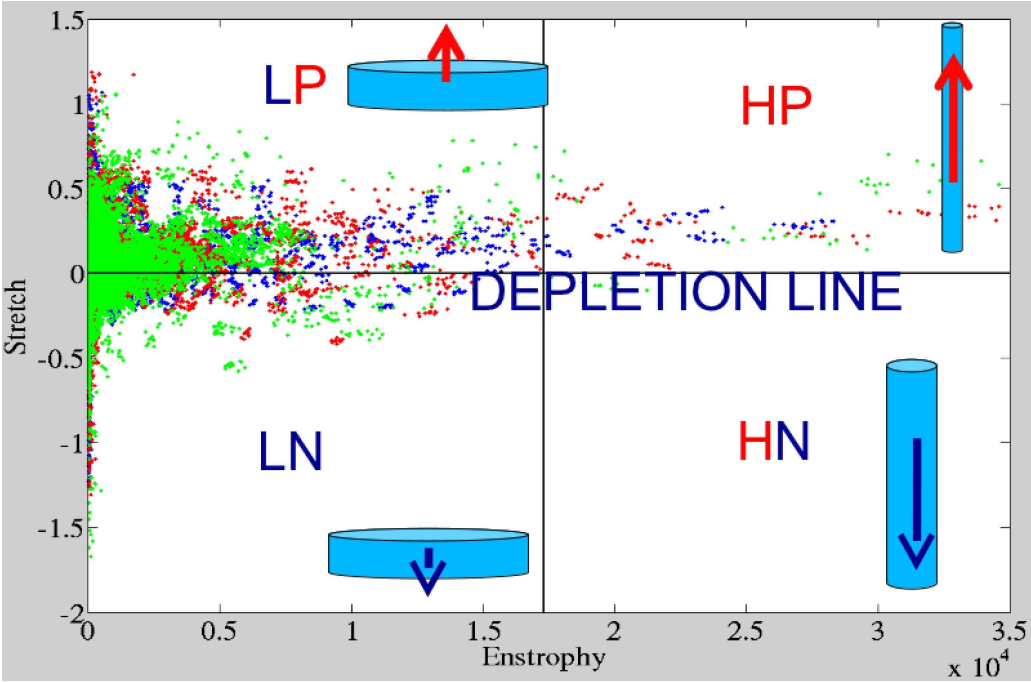

Figure 3.23: Stretching versus Enstrophy scatterplot (enstrophy phase-space) for the case of the KP vortex at $t = 2.15$ (blue), $t = 2.175$ (red) and $t = 2.2$ (green) for Re $= 1000$ with 512^3. The local stretching $s(x, y, z)$ identifies with the (signed) growth rate of a the local enstrophy $\Omega(x, y, z)$.

figure all points located on the vertical line $\Omega = Const.$ belong to the same iso-vorticity contour $|\omega|(x, y, z) = Const.$ The horizontal axis, $s = 0$, defines the neutral "depletion line". The figure demonstrates that the peak of enstrophy is associated with the population of the high-vorticity quadrants, with a (non-exclusive) prevalence of growing structures. The figure also shows that the extremal dynamics is entirely dictated by HP's, as no HN event can be found beyond approximately $\Omega \sim 2$.

LN are the weakest structures, the ones most in danger of disappearing, while *HP* stand just for the opposite trend; they are high in vorticity and still growing. They would absorb the entire enstrophy budget upon untamed growth. The other two, *LP* and *HN*, are in principle the carriers of stable behavior. As witnessed by the iso-surfaces shown in the figure 3.20, such four structures strongly intermix as a consequence of the complex structural dynamics of vorticity tubes(see Supplementary Movie 2). Though the HP structures are the energetic ones with high vorticity, interestingly, the highest stretch is realized by the LP events, which feature $s_{max} \sim 1$. However, the HN's are very ephemeral, as they quickly decay into LN's. If only in descriptive terms, this

population-dynamics schematization indicates that the blow-up scenario would correspond to a complete decoupling of the HP population from the other three, a literal form of untamed enstrophy growth.

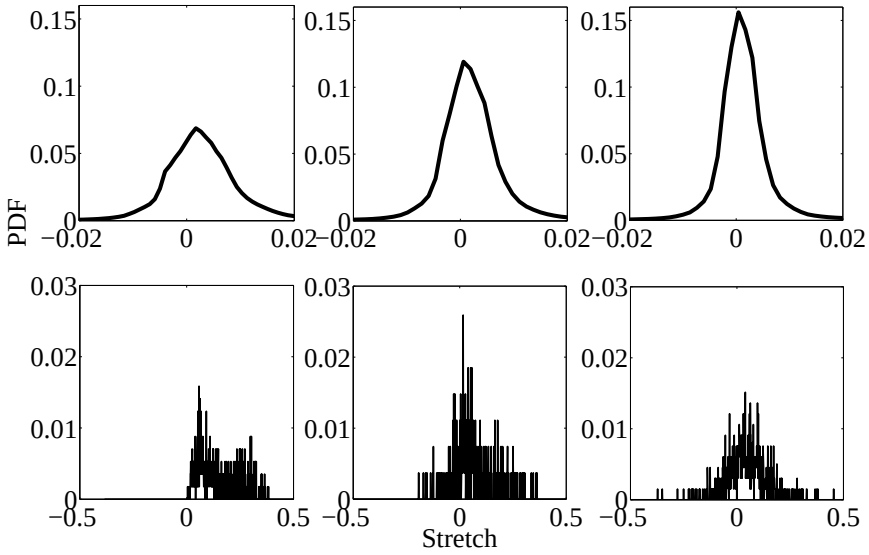

Figure 3.24: Probability distribution of the local stretch in the LV($< \omega_{max}/2$, normalized by the total number of events in LV) (top) and HV($> \omega_{max}/2$) (bottom) regions, respectively, at $t = 2.0$ (left), $t = 2.1$ (middle) and $t = 2.2$ (right) of KP flow at $\mathrm{Re} = 10^4$, with 1536^3.

Figure 3.24, reports the probability distribution function (PDF) of the stretch s in the Low-Vorticity (LV) and High-Vorticity (HV) regions for the KP flow. The figure demonstrates a bell-shaped distribution of both positive and negative growth populations in the LV and HV sectors, with a mild prevalence of positive ones, realizing a positive average stretch. This is shown in figure 3.25, where iso-contours of stretch, with positive and negative stretch, are shown during the initial evolution time. The bell shaped form of the distribution demonstrates that non-linear depletion, $s \approx 0$, is indeed taking place in the system. The distribution in the HV sector is very rough, due to the much smaller number of HV counts, roughly 0.01%, as compared to the LV ones. The substantial shift towards positive growth, is nevertheless quite visible in both cases. The mean growth rate is positive in both cases, with a substantial increase in the HV regions, where the PDF shows a neat shift towards positive s. Visual inspection of the iso-vorticity contours in figure 3.20 proves fully consistent with the above picture.

It is observed that at *any* value of the enstrophy, the LV region contains both positive and negative growth rates, indicating a coexistence of growing and decaying subregions (LP and LN), within the same iso-vorticity surface(figure 3.20). The bulk population in the LV region is centered around the "depletion line", $s = 0$, with a prevalence of mildly positive stretch. A progressive shift towards larger positive s is observed while moving towards the HV region. By and large, the bulk of the events happen around the region $|s| \leq 0.1$, thereby supporting the picture of non-linear depletion as seen in figure 3.22. It also observed that at all times, the LV sector is vastly populated than the HV sector. The latter is populated only around the outburst of the enstrophy peak, as shown in the figure 3.26, through both HP and HN populations, contributing nonetheless four orders of magnitude less events than the LV populations. In spite

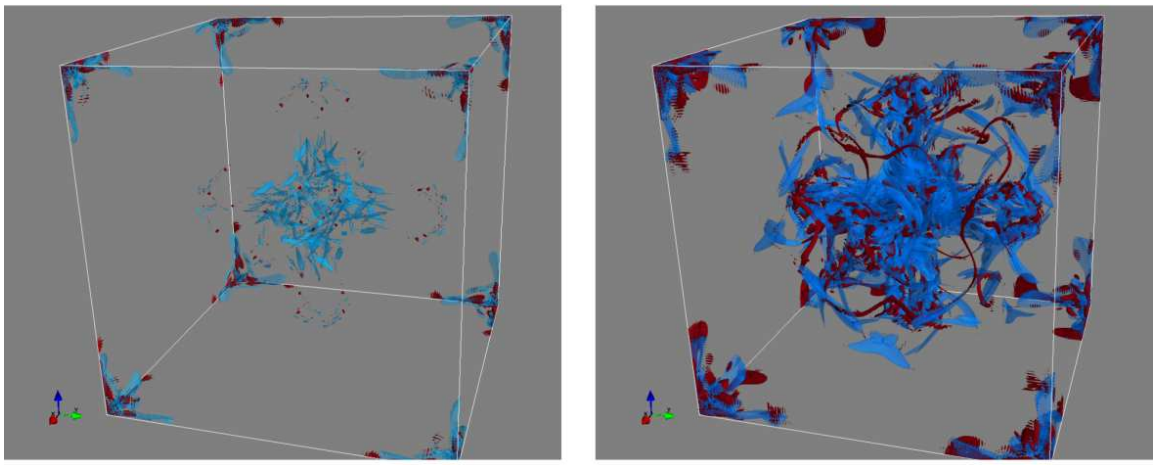

(a) (b)

Figure 3.25: Iso-contours of stretch in the KP flow for $Re = 2000$, with 768^3 resolution at $t = 1.15$. (**a**)High stretch at $s = 0.11$ with positive (blue) and negative (red) stretching. (**b**)Low stretch at $s = 0.055$ with positive (blue) and negative (red) stretching. Like for vorticity, positive stretch regions dominate the dynamics.

of their paucity in number, these events carry a sizable weight on the overall enstrophy budget, and a dominant one on the local enstrophy peak as shown in figure 3.16, which carries *de facto* their signature. Both HV populations are ephemeral, i.e. they vanish away from the peak interval. However, their lifetime is nonetheless fairly appreciable on the overall time scale of the flow, as it lasts about 0.3 global transit times. Thus the statistics of these populations, show a strong prevalence of (mildly) growing ones, with an outburst of strong growers, right before the vorticity peak, followed by subsequent re-absorption after the peak. Figure 3.26 clearly demonstrates the outburst of HV events around the vorticity peak. The HV structures are formally unstable, in the sense that their lifetime is confined to the time interval around the peak. Away from the peak, the enstrophy evolution is dictated by a dynamic equilibrium between growing and decaying low-vorticity structures, which undergo a few damped oscillations before settling to a steady state. From the above observation, we would like to infer that the blowup around the peak, due to HV structures, might be avoided by interaction with that of LV structures, redistributing the energy. The small scale HV structures interact (collision like events) with large scale LV structures resulting in an inverse energy cascade.

3.6 Movies

The spectral dynamics of the flows explored in this work is best exposed by visual inspection of the attached movies (see supplementary material), as detailed below.

1. **Kida-Pelz** (SupplementaryMovie1-a)

   This movie refers to the KP initial condition at Re = 5000, with a spatial resolution of 1024^3, using a PS code. It shows three plots of maximum vorticity versus time, energy spectrum and Taylor micro-scale Reynolds number versus time, respectively. The $k^{-3} \log k$ scaling (middle plot) in energy spectrum, in relation with the attainment of the first

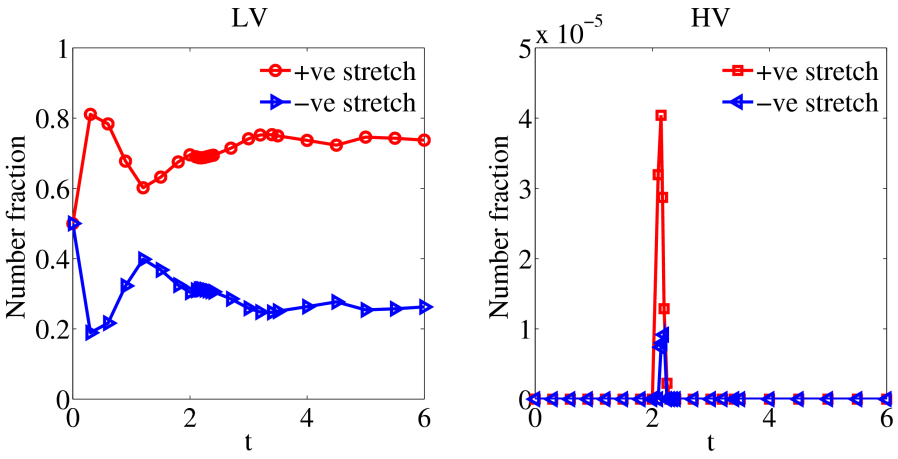

Figure 3.26: Cumulative number and separate enstrophy count in the four quadrants of the scatter plot, as a function of time of KP at $Re = 1000$ with 512^3 resolution.

maximum in maximum vorticity at $t \sim 2.1$, is well apparent in the movie. The spectrum quickly aligns with the $k^{-3} \log k$ line when the first maximum in maximum vorticity is reached, and then moves towards the $k^{-5/3}$ scaling, when the magnitude of maximum vorticity decreases and the flow enters a constant decay stage. The movie runs from $t = 0$ to $t = 10$.

2. **Kida-Pelz** (SupplementaryMovie1-b) There some indication from tracking of maximum vorticity that vorticity saturation is driven by collision-like events among high vorticity blob (0.9 of maximum vorticity at a given time, shown in movie in yellow color) and low vorticity blobs (0.5 of maximum vorticity at a given time, shown in movie in green color). It is also shown that the high vorticity zones are initially not only getting more and more stretched but also approach each other in the central core of the box. However, before high vorticity zone come very close to each other, their interaction with low vorticity object (termed by us as collision) manage to stop the growth of vorticity magnitude. This movie clearly shows that, near t = 2.1, collision-like events are dominant. The snapshots of the movie at various instants is plotted in the figure 3.27.

3. **Taylor-Green** (SupplementaryMovie2)

   Like the previous one, this movie shows the simulation result of TG initial condition at Re $= 5000$ and $N = 1024^3$, from $t = 0$ to $t = 12$, using a PS code. Unlike the KP flow, the maxima in maximum vorticity is attained at $t \sim 6.5$, where the $k^{-3} \log k$ scaling is observed. From the movie, it is also evident that the global maximum in maximum vorticity is reached long after the first local maximum. The flow then goes towards the steady decay, where $k^{-5/3}$ scaling in energy spectrum is observed.

4. **Hill's Vortices** (SupplementaryMovie3)

   This movie refers to the simulation of a group of six Hill's vortices, one from center of each side, colliding at the center of the periodic box. This initial condition is different from

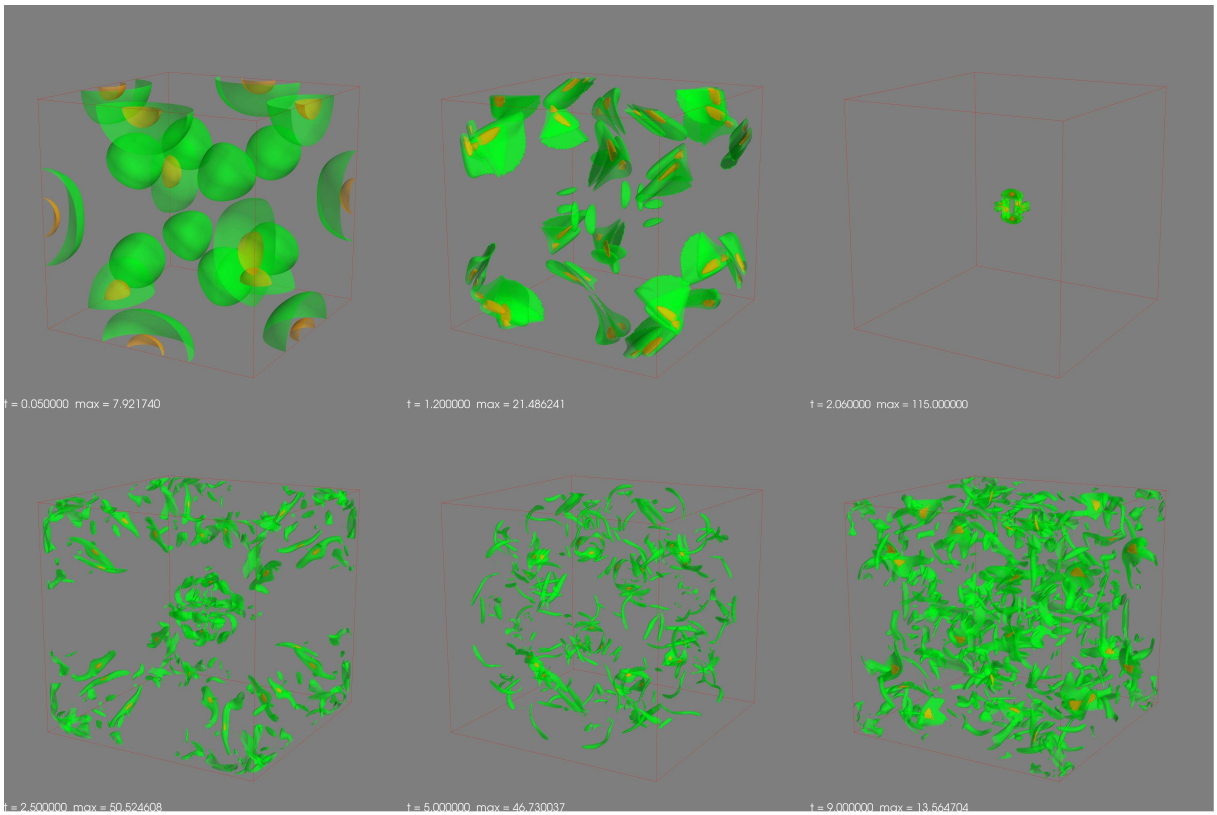

Figure 3.27: Snapshots at t = 0.05, 1.2, 2.06, 2.5, 5.0, 9.0 showing the collision like events at t$\sim$ 2.0 for KP at Re = 1000 and 512^3 resolution

the previous ones, as it shows no symmetry. Notwithstanding this lack of symmetry, the movie confirms the existence of $k^{-3}\log k$ scaling, in accordance with the first maximum of maximum vorticity. It should also be noted that PS methods with periodic boundary conditions cannot represent exactly the jump in vorticity across the boundary of the vortex. This implies a small violation of incompressibility which shows however no appreciable effect on the spectral dynamics of the flow.

3.7 Conclusion

Simulations of decaying turbulence in the range 1000< Re< 10000, with resolution up to 1536^3 are performed. Three different initial conditions namely KP, TG and set of Hill's vortices are used. The results from the simulations suggest that the transient dynamics concurrent with peak in maximum vorticity might be associated with a universal scaling of $k^{-3}\log k$ in energy spectrum. This is accompanied by an inverse energy cascade which suggests a redistribution of energy between high-vorticity small scale structures and low-vorticity large scale structures. The taming of the vorticity might possibly happen due to these interaction (termed collision like events) between high-vorticity positive-stretch and low-vorticity structures. Further, statistical analysis around the peak event shows that the high-vorticity positive structures are avoided from growing any further by moving towards a zero stretch, possibly by local two-dimensionalization.

Chapter 4

Quasiequilibrium lattice Boltzmann models

4.1 Introduction

It was recently shown that for high resolution DNS, the energy conserving lattice Boltzmann models deliver an order of magnitude increase in accuracy, as compared to their athermal counterpart(Singh *et al.* 2011). This was attributed to the absence of unphysical bulk viscosity in the thermal model. However, it was also found that in the under-resolved regime, very often, the athermal model behaves better than the energy conserving model. It can be argued that in under-resolved domain, the high bulk viscosity present in athermal model, helps damping down the acoustic oscillations. Thus, it is natural to wonder whether it would be possible to keep best of both approaches. The aim of the present work is to show that it is indeed possible to design an energy conserving LB model which is efficient in damping acoustic oscillations and thus uniformly better than its athermal counterpart. Part of this work is to appear in International Journal of Modern Physics C (IJMPC).

In section 4.2, we show the empirical observation that models with higher bulk viscosity are better at reducing acoustic perturbations, is consistent with linearized hydrodynamics. Furthermore in section 4.3, we argue that high energy dissipation introduced via low Prandtl number, is also an effective mechanism to damp down the acoustic perturbations and that low Prandtl number simulations are preferable to high bulk viscosity simulations in the non-linear flow regime. Section 4.4 gives the details of the single relaxation LB formulations. In section 4.5, we introduce the multi-relaxation LB with tunable Prandtl number to effectively damp the acoustic fluctuations. From two-dimensional and three-dimensional numerical simulations, we show the advantage of the model discussed over available LB models in section 4.6. Finally we conclude in section 4.7.

4.2 Linear analysis of compressible Navier-Stokes

In this section, we briefly remind the reader about decay of acoustic perturbation in linearized hydrodynamics, governed by (Chaikin *et al.* 2000)

$$\frac{\partial j_\alpha}{\partial t} + \partial_\alpha p - \frac{\eta}{\rho}\nabla^2 j_\alpha - \frac{1}{\rho}\left(\zeta + \frac{\eta}{3}\right)\partial_\alpha \partial_\beta j_\beta = 0 \tag{4.1}$$

where j_{alpha} is momentum, p is pressure, η is the shear viscosity, ρ is density, ζ is bulk viscosity. To this aim, we follow the usual prescription of decomposing the momentum $\mathbf{j}$ into longitudinal

and transverse components as

$$j_\alpha = {j_\alpha}^l + {j_\alpha}^t, \quad \nabla \times \mathbf{j}^l = 0, \quad \partial_\alpha {j_\alpha}^t = 0. \tag{4.2}$$

In this approximation, it is readily shown that the dynamics of the transverse component is fully decoupled from longitudinal component and obeys diffusion equation

$$\partial_t {j_\alpha}^t = \frac{\eta}{\rho} \nabla^2 {j_\alpha}^t, \tag{4.3}$$

Similarly, the longitudinal part of the dynamics can be written as (Chaikin *et al.* 2000)

$$\left[-{\partial_t}^2 + \frac{1}{\rho} \left(\frac{4}{3}\eta + \zeta \right) \partial_t \nabla^2 \right] \delta\rho(\mathbf{x}, t) + \left. \frac{\partial p}{\partial \rho} \right|_S \nabla^2 \delta\rho + \frac{1}{T\rho} \left. \frac{\partial p}{\partial \tilde{s}} \right|_\rho \nabla^2 \tilde{q} = 0, \tag{4.4}$$

where S is the entropy, $\tilde{s}$ is entropy per unit mass, T is the temperature, $\tilde{q}$ is the heat per unit mass and $\partial_t \tilde{q} = \kappa \nabla^2 T(\mathbf{x}, t)$ where κ is thermal conductivity.

This equation can be solved analytically for special initial conditions. A model initial condition for numerical solution is delta perturbation in density. In this case, it is known that any density perturbation decays at a distance r from the disturbance source as (Lifshitz 1987; Ansumali & Karlin 2005),

$$\delta\rho(r, t) = (\mathrm{La}L\, r)^{-\frac{1}{2}} \exp\left(-\frac{(r - c_s t)^2}{2\mathrm{La}L\, r} \right), \tag{4.5}$$

where, L is the characteristic length and La is the Landau number, defined as the ratio of sound propagation timescale (L/c_s) to the viscous dissipation time scale(L^2/ν).

The Landau number can be expressed in terms of the Knudsen number Kn (ratio of Mach number Ma and Reynolds number Re) and the Prandtl number Pr as (Lifshitz 1987)

$$\mathrm{La} = \mathrm{Kn}(2 - \frac{2}{D} + \lambda) + \frac{\mathrm{Kn}(\gamma - 1)}{\mathrm{Pr}}, \tag{4.6}$$

where D is the spatial dimension, λ is the ratio of bulk to shear viscosity and γ is the ratio of specific heat at constant pressure and volume.

From this solution, we see that at a given Knudsen number, the density profile becomes increasingly sharper as the bulk viscosity is decreased. It is known that finite-difference discretizations of sharp profiles tend to generate spurious waves. Thus, a possible solution for low-Mach number simulations is to allow for large La, which leads to smoother profile (See Eq. 4.5). In other words, higher bulk viscosity helps in smoothing the profiles. An alternative way of increasing La, is to perform simulations at very low Prandtl number. Physically, this means that acoustic fluctuations die out faster in metals than in gases. Here we remind that the Prandtl number is largely irrelevant to low-Mach number isothermal dynamics, and consequently, customizing it to effectively dampen acoustic waves, appears to offer a viable strategy. However, we must stress that linear hydrodynamics cannot predict which one, whether low-Prandtl number or high bulk viscosity, is to be preferred for numerical simulations.

4.3 Non-Linear Hydrodynamics

In this section, we briefly analyze the effect of non-linear terms on the previously discussed issues. The nonlinear term in momentum balance equation is given by

$$\begin{aligned}\partial_\beta\left(\frac{j_\alpha j_\beta}{\rho}\right) &= \partial_\beta\left(\frac{j^l_\alpha j^l_\beta + j^t_\alpha j^t_\beta}{\rho}\right) + j^t_\beta\partial_\beta\left(\frac{j^l_\alpha}{\rho}\right) + \left(\frac{j^t_\alpha}{\rho}\right)\partial_\beta j^l_\beta + j^l_\beta\partial_\beta\left(\frac{j^t_\alpha}{\rho}\right)\\ &= \underbrace{\partial_\beta\left(\frac{j^l_\alpha j^l_\beta + j^t_\alpha j^t_\beta}{\rho}\right)}_{\text{A}} + \underbrace{\epsilon_{\alpha\beta\gamma}\epsilon_{\gamma\theta\kappa}\partial_\beta\left(j^l_\kappa\frac{j^t_\theta}{\rho}\right)}_{\text{B}} + \underbrace{j^t_\beta\partial_\beta\left(\frac{j^l_\alpha}{\rho}\right) + \left(\frac{j^t_\beta}{\rho}\right)\partial_\beta j^l_\alpha + j^l_\alpha\partial_\beta\left(\frac{j^t_\beta}{\rho}\right)}_{\text{C}},\end{aligned} \tag{4.7}$$

where the term {B} does not contribute to the longitudinal dynamics and provides a source for the transverse component evolution equation. Similarly, the term {C}, which is also linear in $\mathbf{j}^l$, shows that there is a contribution from the longitudinal to the transverse part evolution. The choice between low-Prandtl number or high bulk viscosity can be made by observing that the longitudinal and transverse components are coupled in the nonlinear hydrodynamics. In the non-linear regime, unphysical dynamics of longitudinal part (change in bulk viscosity) also affect the transverse part. Therefore, it may be argued that introducing a very high bulk viscosity in the model may corrupt the numerical simulation. This was indeed reported in the recent work, where it was observed that, when resolution is sufficiently high, models with bulk viscosity do not converge to the right solution(Singh *et al.* 2011). Based on the above, we believe that acoustic fluctuations are best controlled by introducing an artificially high thermal conductivity (low-Prandtl number). Here, we remind that the error introduced because of temperature dynamics (driven solely by viscous heating) is at least of second order in momentum.

4.4 Isothermal and thermal LB formulation

The LB method is a real-space, kinetic formulation of the equations of fluid dynamics, based on a minimal Boltzmann equation defined on very limited set of discrete velocities in a regular lattice. Since LB is also described in detail in the current literature (for review see Benzi *et al.* (1992); Chen & Doolen (1998); Succi (2001); Aidun & Clausen (2010)), here we shall simply recall the basic ideas behind the method. In the LB formulation, the fluid is represented by a set of discrete populations $f = \{f_i(\mathbf{x};t)\}$, describing the probability of finding a particle at position $\mathbf{x}$ in the lattice, at time t and with discrete velocity $\mathbf{c}_i$ $(i = 1, \cdots, N)$. Since the particles are grid-bound, the number of discrete velocities, N, also defines the connectivity of the lattice. Therefore the basic variables in LB are the discrete populations f_i defined for a set of discrete velocities $\mathbf{c}_i$ $(i = 1, \cdots N)$. The evolution equations for these discrete populations are in the form

$$\partial_t f_i + c_{i\alpha} f_i = \Omega_i(f), \tag{4.8}$$

where Ω_i is the collision term and it ensures that the dynamics goes to the chosen equilibrium. In the entropic formulation of LB, in order to define equilibrium one begins by assuming the

existence of a discrete H functional (Ansumali *et al.* 2003) in the form

$$H = \sum_{i=1}^{N} \left[f_i \left(\ln \left(\frac{f_i}{w_i} \right) - 1 \right) \right], \qquad w_i > 0, \tag{4.9}$$

where w_i are the normalization weights. Once the lattice H-function is known, the equilibrium f^{eq} can be evaluated as a minimum of the H-function under constraints of local conservation of macroscopic variables such as the mass density, ρ, the momentum density $J_\alpha \equiv \rho u_\alpha$, and the energy which is trace of the pressure tensor $P \equiv \frac{1}{2}\rho u^2 + \frac{D}{2}\rho\theta$, where θ is temperature (in Boltzmann units) and D denotes dimension, are defined as linear combinations of the discrete populations

$$\rho = \sum_{i=1}^{N} f_i, \qquad \rho u_\alpha = \sum_{i=1}^{N} f_i c_{i\alpha} \qquad P = \frac{1}{2}\sum_{i=1}^{N} f_i c_i^2. \tag{4.10}$$

The only difference between isothermal and thermal models is that, in an isothermal model, constraint on energy conservation is relaxed by taking θ=1/3. This formulation of LB, which lacks energy conservation implies a finite bulk viscosity.

In the current work, we refer to the so called D3Q27 model, for which mass, momentum and energy conservation is taken into account. The explicit form of the equilibrium, correct up to $O(u^3)$, reads as follows (Ansumali & Karlin 2005):

$$f_i^{\mathrm{eq}} = \rho\, W_i(\theta) \left[1 + \frac{u_\alpha c_{i\alpha}}{\theta} + \frac{u_\alpha u_\beta}{2\,\theta^2} \left(c_{i\alpha} c_{i\beta} - K_i(\theta)\delta_{\alpha\beta} \right) \right], \tag{4.11}$$

where the temperature-dependent weights are given by

$$W_i(\theta) = (1-\theta)^{\mathrm{D}} \left(\frac{\theta}{2(1-\theta)} \right)^{(c_i/c)^2} \tag{4.12}$$

and we have set

$$K_i(\theta) = \frac{2\mathrm{D}\,\theta^2 + \left(\frac{c_i}{c}\right)^2 (1 - 3\,\theta)}{\mathrm{D}\,(1-\theta)}. \tag{4.13}$$

The latter term reduces to the standard lattice sound speed squared, $c_s^2 = 1/3$, in the limit $\theta \to 1/3$. Also, in the case of $\theta = 1/3$, f_i^{eq} is given by

$$f_i^{\mathrm{eq}} = \rho\, W_i(1/3) \left[1 + 3u_\alpha c_{i\alpha} + \frac{9}{2} u_\alpha u_\beta c_{i\alpha} c_{i\beta} - \frac{3}{2} u_\beta u_\beta \right]. \tag{4.14}$$

The set of discrete populations obeys a discrete evolution equation based on two basic steps: free-streaming and local collisions. This reads as follows

$$\begin{aligned} f_i^*(\mathbf{x}, t + \Delta t) &= f_i(\mathbf{x}, t) + \Omega_i(f(\mathbf{x}, t)), \\ f_i(\mathbf{x}, t + \Delta t) &= f_i^*(\mathbf{x} - \mathbf{c}_i \Delta t, t), \end{aligned} \tag{4.15}$$

where the collision term Ω_i, describes the collisions taking the system towards local equilibrium. For most hydrodynamic purposes, this collision term can be modeled as single-relaxation time,

known as a Bhatnagar-Gross-Krook (BGK) model

$$\Omega_i = \frac{1}{\tau}(f_i^{eq} - f_i). \tag{4.16}$$

It is worth mentioning that both the approaches towards hydrodynamics and the numerical stability of the method, are significantly affected by the details of the collision model. The main advantage of the lattice kinetic representation is that streaming takes place along the straight lines defined by the constant discrete velocities. This is a numerically *exact* operation, regardless of the space-time complexity of the fluid configuration. This stands in sharp contrast with the fluid dynamic representation, in which the fluid momentum is transported by its own fluid velocity, a strongly varying function of space and time in a turbulent flow. Furthermore, collisions are fully local, thus implying excellent amenability to parallel implementations.

In the next section, we describe the entropic quasi-equilibrium procedure to construct collision model with multiple-relaxation times, which offers a significant improvement of the numerical stability of the method.

4.5 Generalized quasi-equilibrium LB formulation

In this section, following the procedure outlined in Ansumali *et al.* (2007), we briefly remind how Prandtl number as an independent parameter is introduced in LB framework via quasi-equilibrium models. In this framework, multi-relaxation time is introduced, via the method of

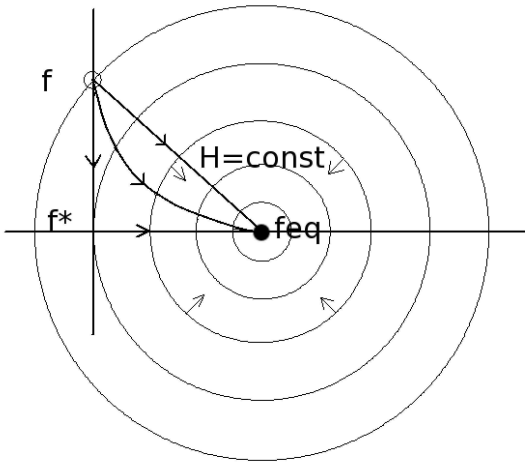

Figure 4.1: Approach to equilibrium in two stages. The quasi-equilibrium, f^*, is found as a minimum of H-function under constraining the quasi-slow variables, and the curved path denotes the relaxation trajectory under the effect of the actual Boltzmann collision integral. In principle, the curved trajectory, could be reproduced by introducing the full spectrum of eigenvalues of the Boltzmann collision operator.

the so-called quasi-equilibrium distribution. As shown in figure 4.1, BGK is a one-step relaxation to equilibrium, while the actual multi-relaxation formulation makes use of an intermediate quasi-equilibrium f^*, (found as a minimum of H-function, under constraints on the additional quasi-conserved variables, such as the energy flux). The two-step relaxation proceeds as follows. First comes a fast relaxation to the quasi-equilibrium state f^*, which is then followed by a slow

relaxation to the equilibrium state f^{eq}. Both relaxation mechanisms are taken in the BGK form, with $\tau \leq \tau_1$ (where τ corresponds to the fast relaxation of f to f^* and τ_1 corresponds to slow relaxation of f^* to f^{eq}) (Levermore 1996; Ansumali *et al.* 2007).

As mentioned above, besides the usual conserved quantities, mass-momentum-energy, also a quasi-conserved one, namely the energy flux (non-equilibrium part), is included in the relaxation process given by

$$\rho = \sum_{i=1}^{N} f_i, \qquad \rho u_\alpha = \sum_{i=1}^{N} f_i c_{i\alpha}, \qquad P = \frac{1}{2}\sum_{i=1}^{N} f_i c_i^2, \qquad \rho q_\alpha = \sum_{i=1}^{N} (f_i - f_i^{eq}) c_i^2 c_{i\alpha}, \tag{4.17}$$

which defines quasi-equilibrium as

$$f_i^* = W_i \exp\left(\alpha + \beta_\theta c_\theta + \gamma c_i^2 + \kappa_\theta c_i^2 c_{i\theta}\right), \tag{4.18}$$

where α, β, γ and κ are Lagrange multipliers.

The two-time relaxation operator in equation (4.8) is given by

$$\Omega_i = \frac{1}{\tau}\left(f_i^*\left(\rho, \mathbf{u}, \theta, \mathbf{q}\right) - f_i\right) + \frac{1}{\tau_1}\left(f_i^{\mathrm{eq}}\left(\rho, \mathbf{u}, \theta\right) - f_i^*\left(\rho, \mathbf{u}, \theta, \mathbf{q}\right)\right). \tag{4.19}$$

The resulting quasi-equilibrium distribution reads as follows,

$$f_i^* = \rho\, W_i(\theta)\left[1 + \frac{c_{i\alpha}}{\theta}\left(u_\alpha - u'_\alpha\right) + \frac{u_\alpha u_\beta}{2\,\theta^2}\left(c_{i\alpha}c_{i\beta} - K_i(\theta)\delta_{\alpha\beta}\right) + \frac{q_\alpha}{(\mathrm{D}-1)\theta^2(1-\theta)} c_{i\alpha} c_i^2\right], \tag{4.20}$$

where we have set

$$u'_\alpha = q_\alpha \frac{1 + (\mathrm{D}-1)\theta}{(\mathrm{D}-1)\theta(1-\theta)}. \tag{4.21}$$

The relaxation time τ fixes the dynamic viscosity μ via usual relation, $\mu = \tau\, p$, while the second relaxation time controls thermal diffusion via the Prandtl number

$$\mathrm{Pr} = \frac{5}{2}\frac{\tau}{\tau_1}. \tag{4.22}$$

There is no additional computational effort required when going from higher to lower Prandtl number. The trade-off is between the accuracy and stability. Although, the actual increase in computational cost is using the multi-relaxation model against a single-relaxation model. Apart from f_i^{eq} only one additional term namely

$$f_i^* - f_i^{eq} = q_\alpha c_{i\alpha} \frac{c_i^2 - (1 + (\mathrm{D}-1)\theta)}{(\mathrm{D}-1)\theta^2(1-\theta)}. \tag{4.23}$$

is to be calculated in the code (from which f_i^* can also be calculated). The kinetic equation Eq.(4.8) is integrated along the characteristics, using the trapezoidal scheme to obtain the following evolution equation:

$$g_i(\mathbf{x} + \mathbf{c}\Delta t, t + \Delta t) = g_i(\mathbf{x}, t)\,(1 - 2\beta) + 2\beta\left[\left(1 - \frac{\tau}{\tau_1}\right) f_i^*\left(\rho, \mathbf{u}, \theta, \mathbf{q}\right) + \frac{\tau}{\tau_1} f_i^{\mathrm{eq}}\left(\rho, \mathbf{u}, \theta\right)\right], \tag{4.24}$$

where g is the auxiliary population defined as,

$$g(\mathbf{x},t) = f(\mathbf{x},t) - \frac{\Delta t}{2}\Omega\left(f(\mathbf{x},t)\right), \qquad \beta = \frac{\Delta t}{2\tau + \Delta t}. \tag{4.25}$$

The moments in terms of the auxiliary population g are given by:

$$\rho(g) = \rho(f),\ u_\alpha(g) = u_\alpha(f),\ T(g) = T(f) \text{ and } q_\alpha(g) = q_\alpha(f)\left(1 + \frac{\Delta t}{2\tau_1}\right). \tag{4.26}$$

4.5.1 Moment chain

The moment chain for the present model is,

$$\begin{aligned}
\partial_t \rho + \partial_\alpha j_\alpha &= 0 \\
\partial_t j_\alpha + \partial_\beta P_{\alpha\beta} &= 0 \\
\partial_t P + \partial_\beta Q_\beta &= 0 \\
\partial_t P_{xy} + \partial_\beta Q_{xy\beta} &= \frac{1}{\tau}\left(\rho u_x u_y - P_{xy}\right) \\
\partial_t P_{xz} + \partial_\beta Q_{xz\beta} &= \frac{1}{\tau}\left(\rho u_x u_z - P_{xz}\right) \\
\partial_t P_{yz} + \partial_\beta Q_{yz\beta} &= \frac{1}{\tau}\left(\rho u_z u_y - P_{yz}\right) \\
\partial_t N_1 + \partial_\beta\left(Q_{xx\beta} - Q_{yy\beta}\right) &= \frac{1}{\tau}\left(\rho(u_x^2 - u_y^2) - N_1\right) \\
\partial_t N_2 + \partial_\beta\left(Q_{xx\beta} - Q_{zz\beta}\right) &= \frac{1}{\tau}\left(\rho(u_x^2 - u_z^2) - N_2\right) \\
\partial_t Q_\beta + \partial_\gamma R_{\beta\gamma} &= \frac{1}{\tau_1}\left(Q_\beta^{\mathrm{eq}} - Q_\beta\right) \\
\partial_t R_{\alpha\beta}\cdots &
\end{aligned} \tag{4.27}$$

where,

$$P = \sum_i f_i c_i^2, \quad N_1 = \sum_i f_i\left(c_{ix}^2 - c_{iy}^2\right), \quad N_2 = \sum_i f_i\left(c_{ix}^2 - c_{iz}^2\right)$$
$$Q_{\alpha\beta\gamma} = \sum_i f_i c_{i\alpha} c_{i\gamma} c_{i\alpha}, \quad Q_\alpha = \sum_i f_i c_{i\alpha} c_i^2, \quad R_{\alpha\beta} = \sum_i f_i c_{i\alpha} c_{i\beta} c_i^2$$

These system of equations are not closed, however unlike moment chain encountered in continuous kinetic theory, this moment chain is always closed due to discrete nature of the model. The underlying hydrodynamics model can be derived using Chapmann-Enskog expansion.

4.5.2 Chapmann Enskog expansion

In order to find the transport coefficients, we perform the Chapmann Enskog (CE) expansion of the present multi-relaxation Prandtl model. Now, following the typical procedure of expanding

time derivative and moments in term of smallness parameter ϵ, we have

$$\begin{aligned}
\frac{\partial}{\partial t} &= \frac{\partial^{(0)}}{\partial t} + \epsilon \frac{\partial^{(1)}}{\partial t} \\
P_{\alpha\beta} &= P^{\mathrm{eq}}_{\alpha\beta} + \epsilon P^{(1)}_{\alpha\beta} \\
N_1 &= N^{\mathrm{eq}}_1 + \epsilon N^{(1)}_1 \\
N_2 &= N^{\mathrm{eq}}_2 + \epsilon N^{(1)}_2 \\
Q_{\alpha\beta\gamma} &= Q^{\mathrm{eq}}_{\alpha\beta\gamma} + \epsilon Q^{(1)}_{\alpha\beta\gamma} \\
Q_{\alpha} &= Q^{\mathrm{eq}}_{\alpha} + \epsilon Q^{(1)}_{\alpha} \\
R_{\alpha\beta} &= R^{eq}_{\alpha\beta} + \epsilon R^{(1)}_{\alpha\beta},
\end{aligned} \tag{4.28}$$

$$\begin{aligned}
-P^{(1)}_{xy} &= \partial^{(0)}_t P^{eq}_{xy} + \partial_\gamma (Q^{eq}_{xy\gamma}) \\
&= \partial^{(0)}_t (\rho u_x u_y) + \partial_x (\underbrace{Q^{eq}_{xyx}}_{\rho u_y T}) + \partial_y (\underbrace{Q^{eq}_{xyy}}_{\rho u_x T}) + \partial_z (\underbrace{Q^{eq}_{xyz}}_{0}) \\
&= -u_x \partial_y (\rho T) - u_y \partial_x (\rho T) + \partial_x (u_y \rho T) + \partial_y (u_x \rho T) \text{ Neglecting higher order term in } \mathbf{u} \\
&= \rho T \left(\partial_x u_y + \partial_y u_x \right)
\end{aligned} \tag{4.29}$$

It means

$$\begin{aligned}
P_{xy} &= -\rho T \left(\partial_x u_y + \partial_y u_x \right) \\
P_{xz} &= -\rho T \left(\partial_x u_z + \partial_z u_x \right) \\
P_{yz} &= -\rho T \left(\partial_z u_y + \partial_y u_z \right)
\end{aligned} \tag{4.30}$$

Finally,

$$\begin{aligned}
-N^{(1)}_1 &= \partial^{(0)}_t N^{eq}_1 + \partial_\gamma (Q^{eq}_{xx\gamma}) \\
&= \partial^{(0)}_t (\rho u_x^2 - \rho u_y^2) + \partial_x (\underbrace{Q^{eq}_{xxx} - Q^{eq}_{yyx}}_{3Tu_x - \rho u_x T}) + \partial_y (\underbrace{Q^{eq}_{xxy} - Q^{eq}_{yyy}}_{\rho u_y T - 3 u_y T}) + \partial_z (\underbrace{Q^{eq}_{xxz} - Q^{eq}_{yyz}}_{0}) \\
&= -2u_x \partial_x (\rho T) - 2u_y \partial_y (\rho T) + 2\partial_x (u_x \rho T) + 2\partial_y (u_y \rho T) \\
&= 2\rho T \left[\rho T \partial_x (u_x) - \rho T \partial_y (u_y) \right] \\
N^{(1)}_1 &= -2\rho T \left[\partial_x (u_x) - \partial_y (u_y) \right]
\end{aligned} \tag{4.31}$$

Similarly,

$$N^{(1)}_2 = -2\rho T \left[\partial_x (u_x) - \partial_z (u_z) \right] \tag{4.32}$$

Hence, we have,

$$P^{\mathrm{neq}}_{\alpha\beta} = P_{\alpha\beta} - P^{\mathrm{eq}}_{\alpha\beta} = \tau \rho T \left(\partial_\alpha u_\beta + \partial_\beta u_\alpha - \frac{2}{3} \delta_{\alpha\beta} \partial_\gamma u_\gamma \right) \tag{4.33}$$

which gives shear viscosity as $\mu = \tau \rho T$

Now,

$$\begin{aligned}\frac{-\epsilon}{\tau_1}Q_x^{(1)} &= \partial_t^{(0)}(Q_x^{\text{eq}}) + \partial_x R_{xx}^{\text{eq}} + \partial_y R_{xy}^{\text{eq}} + \partial_z R_{xz}^{\text{eq}} \\ &= 2\rho T\partial_x T + \quad \text{terms containing } \mathbf{u} \\ Q_x^{(1)} &= \frac{\tau_1}{-\epsilon}2\rho T\partial_x T + \text{.....with } \epsilon \to \tau \text{ since } \tau \leq \tau_1\end{aligned} \tag{4.34}$$

Putting the about expression in energy equation, we get

$$Q_x^{\text{neq}} = Q_x - Q_x^{\text{eq}} = -\tau_1 \rho T \partial_x T \tag{4.35}$$

Hence thermal conductivity in this case is $\tau_1 \rho T$ which was $5/2\tau\rho T$ in the continuous case. Therefore Prandtl number Pr is given by

$$Pr = \frac{5}{2}\frac{\tau}{\tau_1} \tag{4.36}$$

4.6 Results

We demonstrate the superiority of the Prandtl model over the iso-thermal and energy conserving LB model using three two dimensional simulations namely, density perturbation in a quiescent fluid, TG flow and double periodic shear layer. As a three dimensional validation we provide simulation results of KP flow with other standard methods.

4.6.1 Density perturbations in two-dimensions

In order to support the discussion in section 4.2, we have carried out numerical simulations to analyze the density perturbations with different LB schemes. The initial condition is a uniform velocity (u = 0.05, v = 0.05) and density ($\rho = 1.0$) throughout the domain except at the center where the density is perturbed($\delta\rho = 0.01$). This initial condition is simulated with isothermal, thermal and quasi-equilibrium (with variable Pr) LB methods with a grid size of 200×200 and Re = 100. To show the acoustic damping behavior of various methods we show the L_2 norm of the density perturbation in the domain after 100 iterations with varying La (not directly but by varying Kn and Pr). Figure 4.2(left) qualitatively shows the density fluctuations in the domain with initial condition given above after 100 iterations. The La number (see eqn 4.6) for isothermal, thermal and Prandtl models considering $\lambda = \{2/3,\ 0,\ 0\}$,$\gamma = 5/3$ and Pr = {4, 4, 0.1} are {11/6 Kn, 7/6 Kn, 46/6 Kn } respectively where Kn = 1.73×10^{-4}. The figure shows that the density fluctuations indeed decrease with increasing La number. To quantify the results obtained, these simulations are performed with varying Kn, shown in figure 4.3 (left), to quantify the effect of La in damping the acoustic fluctuations. As expected the acoustic fluctuations in the domain decrease with increasing Kn. Further, the quasi-equilibrium (or Prandtl model) LB simulation is run with the least of the Kn (1.73×10^{-4}) used in other two methods (i.e with lowest damping of oscillations), but with varying Pr effectively changing the La. The results of the simulation are shown in figure 4.3 (right) which are supportive of the fact that density perturbations decay faster with decreasing Pr number. It should be noted that beyond a certain

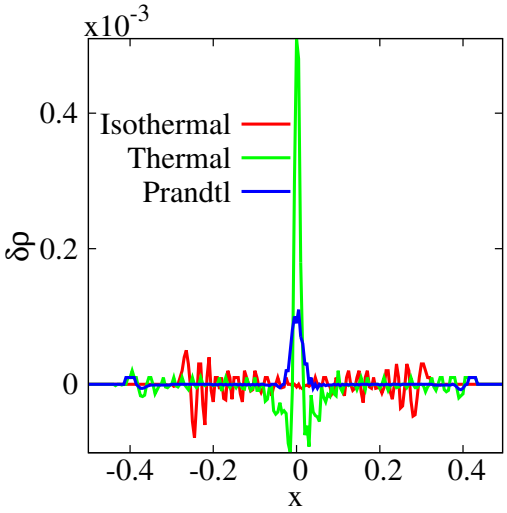

Figure 4.2: Variation of density fluctuation with x with same Kn for the three LB methods discussed.

limit decreasing Pr number any further would result in deteriorating the results.

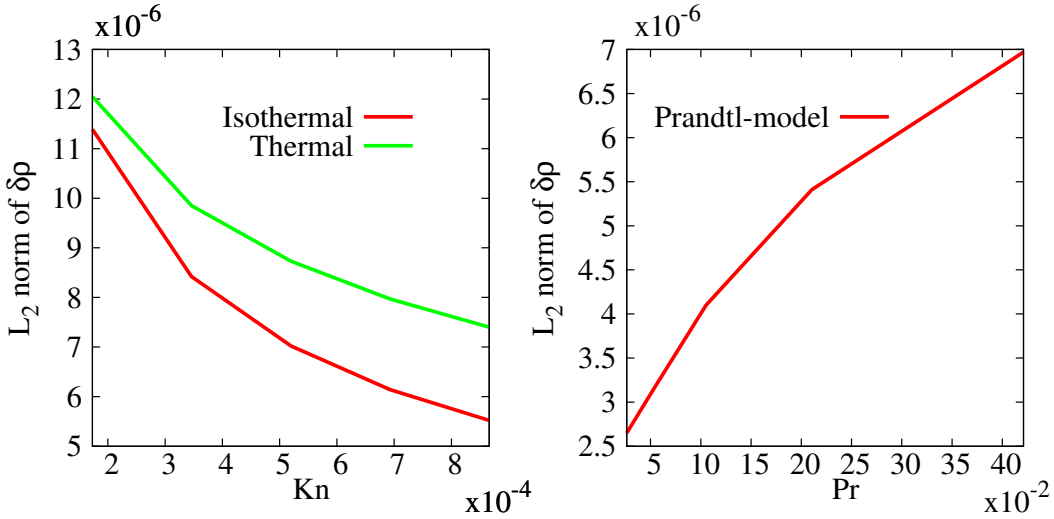

Figure 4.3: (**Left**)Variation of L_2 norm of density fluctuation with Kn at a fixed Pr. (**Right**)Variation of L_2 norm of density fluctuation with Pr at a fixed Kn.

4.6.2 Two dimensional Taylor-Green vortex

To further validate our method, we have chosen the Taylor-Green vortex simulation as a model problem, in order to analyze the behavior of an isothermal (with a finite bulk viscosity), thermal(energy-conserving) and quasi-equilibrium model with tunable Prandtl number. Since there is no boundary effects, the error analysis reveals the accuracy of different models. This set up was analyzed earlier, to compare isothermal and energy conserving LB (Singh *et al.* 2011). In order to compare the performance of the current model with that of Singh *et al.* (2011), we

performed a grid resolution study for the velocity profile whose analytic solution is given by

$$\begin{aligned} u(x,y,t) &= \sin x \cos y \, e^{-2\nu t} \\ v(x,y,t) &= -\cos x \sin y \, e^{-2\nu t} \end{aligned} \tag{4.37}$$

along the x direction at a fixed Mach (Ma) and Reynolds (Re) numbers. Here, Ma number is defined as Ma $= \mathrm{U}_0/\mathrm{c_s}$ and Re is based on the characteristic length of the flow-field, taken as 1 in a periodic-box of length $2\,\pi$, thus Re $= U_0/\nu$. As the Prandtl number is just a tunable parameter in the current study, all our simulations have used Prandtl number Pr $\propto \sqrt{\mathrm{Kn}}$ and Kn and La is completely dictated by behavior of Pr. In the current simulations of Taylor-Green flow, we have chosen $\sqrt{\mathrm{Kn}} = 0.0014$. As shown in figure 4.4, even at low grid resolution, the model with a change in Pr, with different τ/τ_1 (here, Pr=$4\tau/\tau_1$), provides a more accurate simulation of the Taylor-Green vortex, in comparison to isothermal model (except at a very poorly resolved regime). This result reinforces the fact that the longitudinal and transverse components of momentum are indeed coupled, and varying Pr is a better choice than changing the bulk viscosity.

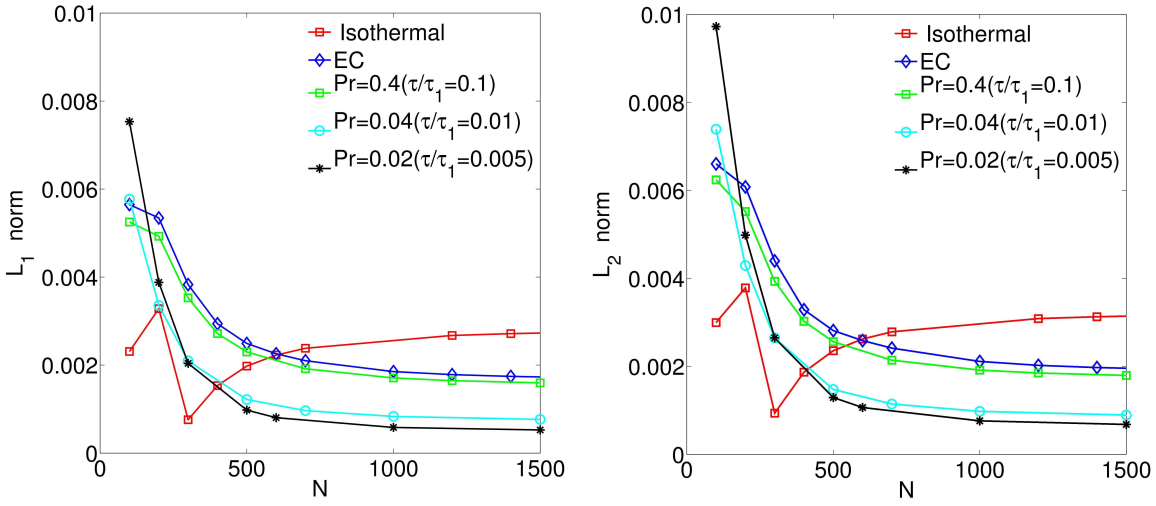

Figure 4.4: L_1 and L_2 norm for velocity in x direction at $Re = 4000$ and Ma $= 0.05$ for Taylor-Green vortex with different grid size.

4.6.3 Two dimensional double periodic shear layer

To demonstrate the method qualitatively, we consider the set up of doubly periodic shear layer in two-dimensions (Brown & Minion 1995) given by

$$\begin{aligned} u(x,y,0) &= \begin{cases} tanh(\kappa(y-1/4)), & y \le 1/2, \\ tanh(\kappa(3/4-y)), & y > 1/2, \end{cases} \\ v(x,y,0) &= \delta sin(2\pi(x+1/4)) \end{aligned} \tag{4.38}$$

where κ varies the thickness of the shear layer and δ is the magnitude of the initial perturbation induced in the simulation. Figure 4.5 shows the vorticity contours of this initial condition.

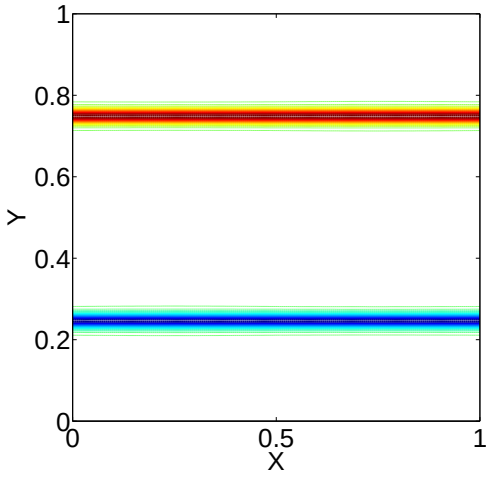

Figure 4.5: Iso-contours of vorticity field for double periodic shear layer initial condition

Due to the Kelvin-Helmholtz instability triggered by the perturbation in the initial shear layers, they roll up and move in the domain. This initial condition is sensitive to the computational method used because of the presence of large velocity gradients in the domain. Thus, this initial condition permits a stringent comparison between various methods, both in terms of stability and accuracy. In present simulation as a representative example of high Re, low Ma flow we choose Re = 30000, Ma = 0.0693 ($U_0 = 0.04$) for isothermal as well as for simulations with Prandtl model. The ratio between two time scales in the latter i.e. τ/τ_1, is taken to be 0.005 and in this case $\sqrt{Kn} = .00152$. Figure 4.6 shows that the Prandtl model is stable, while the athermal model blows up at a given lower resolution setup. This simple qualitative comparison shows that the range of applicability of Pr model is more than that of isothermal model, in sub-grid domain, in term of stability. It can be seen from figure 4.7, that the setup with Prandtl correction converges towards a steady state value at a higher grid resolution, similar to isothermal setup.

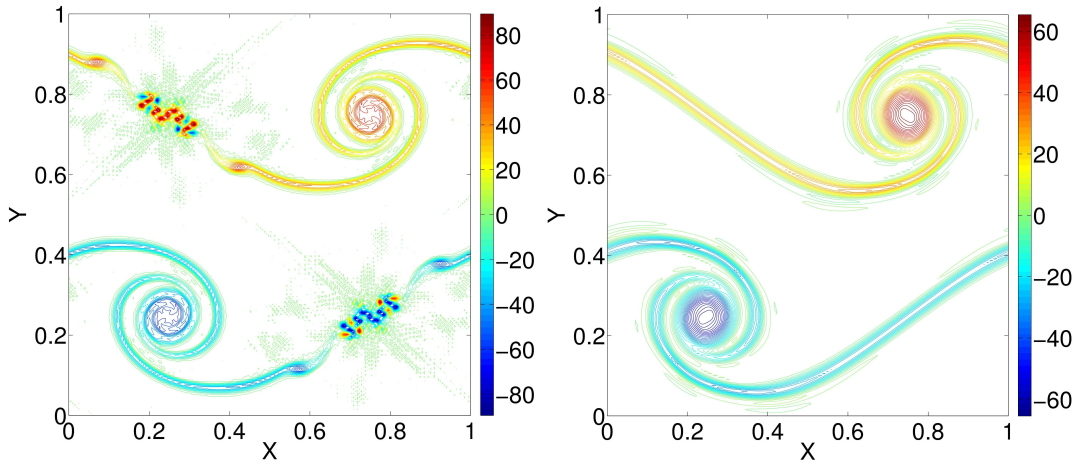

Figure 4.6: Vorticity field at time=1 on 200×200 grid for athermal (left) and Prandtl (right) models at Re = 30000, Ma = 0.04.

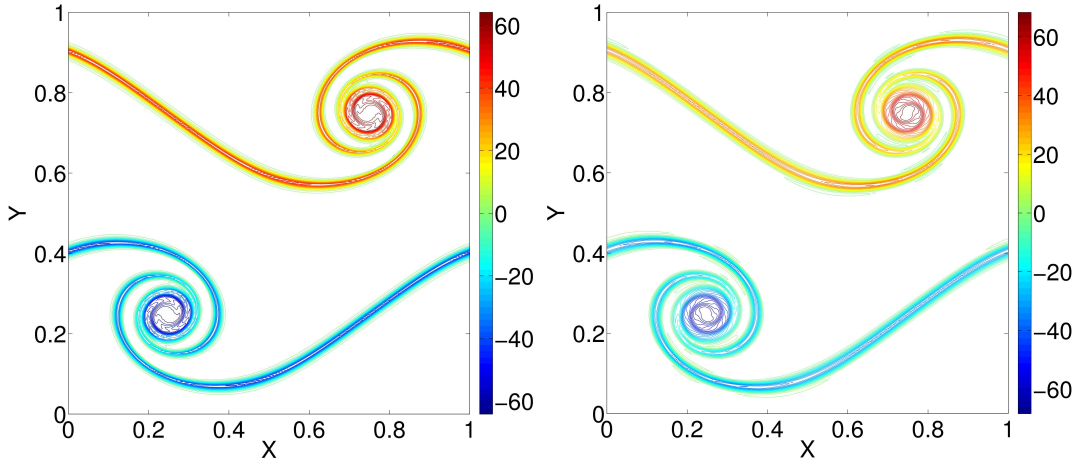

Figure 4.7: Vorticity field at time=1 on 312×312 for athermal (left) and Prandtl (right) at Re = 4000, Ma = 0.05.

4.6.4 Three-dimensional benchmark simulations

As a further stringent test for the current formulation, we use KP flow discussed in the previous chapter. These simulations are compared with the results obtained from the pseudo-spectral code. In order to show the accuracy of the present formulation, we compare various physical quantities, like enstrophy and maximum vorticity. As LB is a primitive formulation of hydrodynamics, vorticity is not directly accessible in LB simulations. However, the energy and enstrophy can be calculated on the fly, without taking any spatial derivative. We remind that enstrophy can be computed from the symmetric velocity gradient tensor (Frisch 1995), which is available in LB simulations locally via

$$S_{\alpha\beta} = \frac{2}{\rho T(2\tau + \Delta t)} \sum_i (f_i^{\mathrm{eq}} - f_i)\, c_{i\alpha} c_{i\beta}, \qquad \tau = \frac{\nu}{c_s^2}. \tag{4.39}$$

Note that this expression which is based on CE expressions, does not require the calculation of any explicit spatial derivative.

The results show a good agreement between the LB and PS methods. Enstrophy shown in figure 4.8, which is more sensitive to the numerical resolution than the kinetic energy, is compared in both PS and LB. The figure shows the behavior of various methods at different resolutions. It is evident from the figure that the Pr model captures the peaks better than other LB models assuming that the PS result is most accurate one among them.

Maximum vorticity which is the infinite norm of vorticity in the entire domain at a given instant is tracked in time as shown in figure 4.9. This quantity is more sensitive to the grid resolution than the enstrophy, which is an average quantity over the domain. From this figure we infer that we are still working in the sub-grid domain and that the Pr model is better or as good as the other methods.

Longitudinal and transverse correlations of the velocity field are important quantities to show the variation, in terms of accuracy, of different numerical techniques. These quantities are

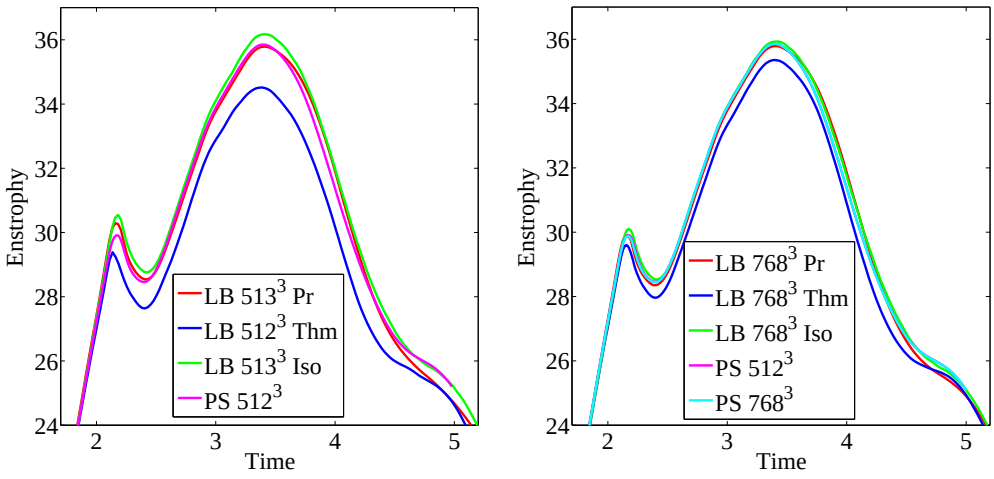

Figure 4.8: Comparison of Enstrophy for Kida flow at Re = 1000 using D3Q27.

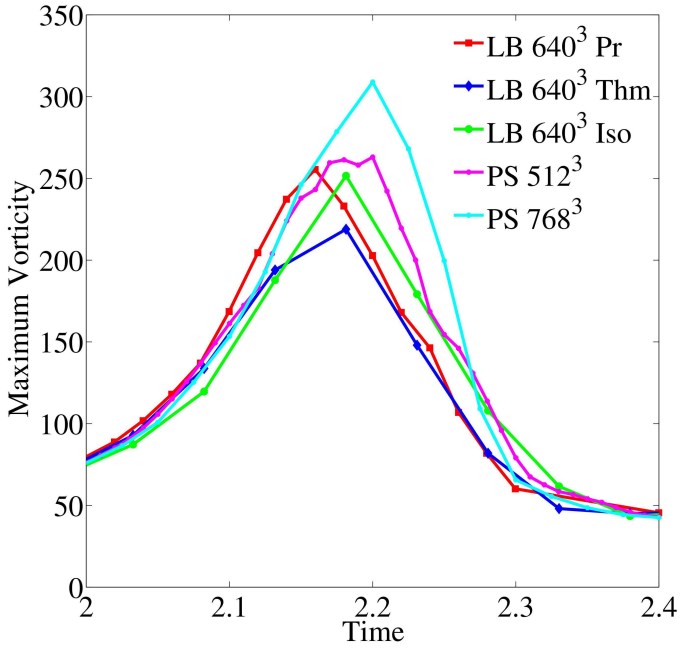

Figure 4.9: Comparison of maximum vorticity for Kida flow at Re = 1000.

given by

$$\rho_{11}(r) = \frac{\langle u_x(x,y,z)\, u_x(x+r,y,z)\rangle}{\langle u_x(x,y,z)\, u_x(x,y,z)\rangle}$$
$$\rho_{22,33}(r) = \frac{\langle u_{y,z}(x,y,z)\, u_{y,z}(x+r,y,z)\rangle}{\langle u_{y,z}(x,y,z)\, u_{y,z}(x,y,z)\rangle} \tag{4.40}$$

Figure 4.10 shows a good agreement of the Prandtl model in comparison with the PS results. Thus, Prandtl model could capture these velocity correlations effectively.

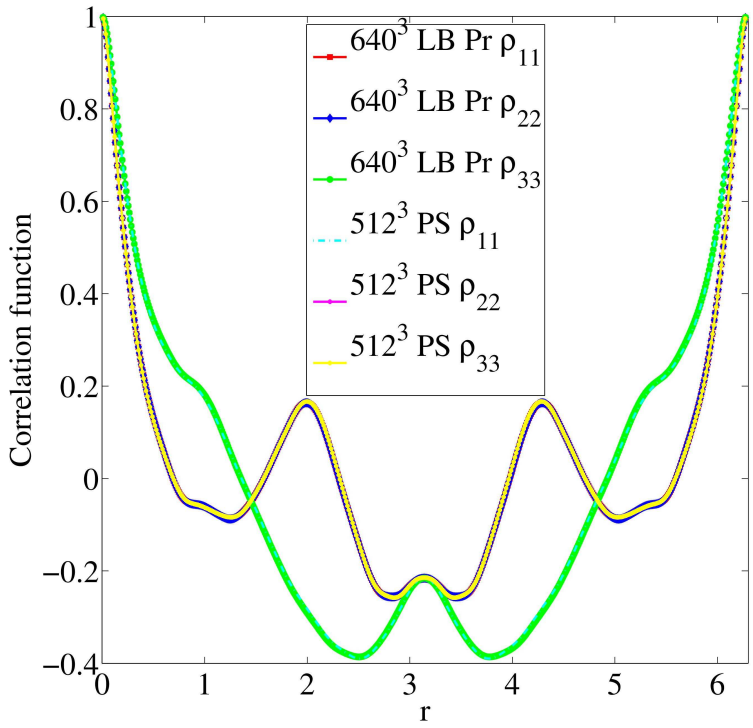

Figure 4.10: Comparison of velocity correlations for KP flow at Re = 1000.

4.7 Conclusion

The multi-relaxation LB method with tunable Prantl number gives consistent performance in both sub-grid and fully resolved regimes. However, a more quantitative study is needed to compare efficiency of LB as compared to PS method in massively parallel environments. The sub-grid and well resolved simulation results, obtained with the Prandtl model are superior to both isothermal and energy conserving models. It implies that this model is stable than isothermal in sub-grid domain and as accurate as energy conserving model in fully resolved simulations. Thus present formulation increases the utility of LB as a tool for sub-grid simulation.

Chapter 5

Summary and conclusions

High-resolution pseudo-spectral simulations performed in this thesis, suggest that the saturation of vorticity growth in non-equilibrium transients of homogeneous, incompressible turbulence, might be associated with a universal scaling of $k^{-3}\log k$ in energy spectrum. The attainment of such universal transient state is signaled by an intense outburst of high-vorticity and positive-stretch, structures, whose signature manifests in the form of a clearcut peak in the maximum vorticity. The statistical distribution of the growth rates indicates coexistence of decaying and growing subregions on each given iso-vorticity surface. We speculate that the aforementioned universal mechanism might be the result of a built-in vorticity redistribution policy, whereby the high vorticity structures are prevented from running away by direct interaction with the low-vorticity ones. Further, the third order structure function suggests an inverse energy cascade which suggests interactions between high-vorticity small scale structures and low-vorticity large scale structures. The two-dimensional-like $k^{-3}\log k$ spectrum in the peak stage of vorticity growth might be associated with local two-dimensionalization as suggested by visual inspection of the flow morphology and statistical analysis of the local growth rates on each iso-vorticity surface. Based on the present simulations, we believe that viscosity would not play any significant role on the physical picture portrayed in this work. The picture presented in this work is entirely based on simulation evidence yet to be developed into a quantitative mathematical model. Finally, while the occurrence of similar behavior across three different types of flows sets a strong pointer to universality, further explorations are certainly needed to verify the conjecture of universality.

The new energy conserving lattice Boltzmann scheme, Prandtl method, allows to extend the accuracy to lower resolutions, where conventional energy conserving LB schemes are known to yield poorer results than their athermal counterparts. Prandtl number plays a sub-dominant role in low-Mach number isothermal flows so that it can be used as a free tuning parameter to optimize numerical accuracy and stability via efficient damping of the sound modes. Thus, the Prandtl number is a better parameter to tune over the bulk viscosity in multi-relaxation LB models. Various simulations have been performed which show the superiority of the Prandtl model over both iso-thermal and energy conserving LB methods. We have shown that it is possible to preserve the accuracy of the energy conserving lattice Boltzmann for both sub-grid and high resolution DNS regime. The Prandtl scheme is more stable than the athermal model in sub-grid domain, and it converges to the results of thermal model at higher resolutions.

Appendix A

Computational Resources

Due to the relentless advances of computing technology in the recent years, computational fluid dynamics simulations with billions of degrees of freedom are now feasible at the level of individual groups, with no need of accessing top supercomputing platforms. Most of the present simulations were performed on a 13-node, heterogeneous cluster, based on the resources available in early 2010 in our lab, namely 4 nodes of 16 processors (AMD Opteron(tm) Processor 6136), with 32 GB RAM (DDR3) each and 9 nodes of 12 processors (Six-Core AMD Opteron(tm) Processor 2439 SE), with 64 GB RAM (DDR2) each, connected by a infiniband switch, providing interconnect speed of about 10 Gb/s. The peak performance of this system is slightly above 1 Teraflop, with a total RAM availability of about 896 GB. In fact, the technology change is drastic enough, that some of the largest simulations performed in the later part of this work, were actually run on a high-end single server. This system has single node with 32 processors (4×8 Intel Xeon processors E7-4830) with DDR3 RAM of 128 GB and approximate peak performance of 0.25 Teraflop.

The minimum system size used in our simulations was 48 million degrees of freedom, (a spectral run with 512^3 system size, where symmetry was used). We remind that for N^3 fluid points simulated with first octant only would have degree of freedom equals to $N^3 \times 8/3$.

The largest PS run was with 1.26 **billion** degrees of freedom (with symmetry), while the largest LB simulation was with 27 billion degrees of freedom, corresponding to a grid size 1000^3, each lattice site point hosting 27 double-precision variables.

References

Aidun, C. K. & Clausen, J. R. 2010 Lattice-boltzmann method for complex flows. *Annual Review of Fluid Mechanics* **42**, 439–472.

Aivazis, K. A. & Pullin, D. I. 2001 On velocity structure functions and the spherical vortex model for isotropic turbulence. *Phys. Fluids* **13**, 2019–2029.

Ansumali, S., Arcidiacono, S., Chikatamarla, S., Prasianakis, N. I., Gorban, A. N. & Karlin, I. V. 2007 Quasi-equilibrium lattice boltzmann method. *The European Physical Journal B-Condensed Matter and Complex Systems* **56** (2), 135–139.

Ansumali, S. & Karlin, I. V. 2005 Consistent lattice Boltzmann method. *Phys. Rev. Lett.* **95** (26), 260605.

Ansumali, S., Karlin, I. V. & Öttinger, H. C. 2003 Minimal entropic kinetic models for simulating hydrodynamics. *Europhys. Lett.* **63**, 798–804.

Ansumali, S., Karlin, I. V. & Succi, S. 2004 Kinetic theory of turbulence modeling: smallness parameter, scaling and microscopic derivation of smagorinsky model. *Phys. A: Stat. Mech and App* **338** (3), 379–394.

Asinari, P. & Karlin, I. V. 2010 Quasiequilibrium lattice boltzmann models with tunable bulk viscosity for enhancing stability. *Physical Review E* **81** (1), 016702.

Benzi, R., Succi, S. & Vergassola, M. 1992 The lattice boltzmann equation: theory and applications. *Phys. Rep* **222** (3), 145–197.

Bespalko, D. J. 2011 Validation of the lattice boltzmann method for direct numerical simulation of wall-bounded turbulent flows .

Boratav, O. N. & Pelz, R. B. 1994 Direct numerical simulation of transition to turbulence from a high-symmetry initial condition. *Phys. Fluids* **6**, 2757.

Boratav, O. N. & Pelz, R. B. 1995 On the local topology evolution of a high-symmetry flow. *Phys. Fluids* **7**, 1712.

Boratav, O. N. & Pelz, R. B. 1997 Structures and structure functions in the inertial range of turbulence. *Phys. Fluids* **9**, 1400.

Boyd, J. P. 2001 *Chebyshev and Fourier spectral methods*. Courier Dover Publications.

Brachet, M. E., Meiron, D. I., Orszag, S. A., Nickel, B. G., Morf, R. H. & Frisch, U. 1983 Small-scale structure of the Taylor-Green vortex. *J. Fluid Mech.* **130** (41), 1452.

Brown, D. L. & Minion, M. L. 1995 Performance of under-resolved two-dimensional incompressible flow simulations 1 p .

Bustamante, M. D. & Brachet, M. 2012 Interplay between the beale-kato-majda theorem and the analyticity-strip method to investigate numerically the incompressible euler singularity problem. *Phys. Rev. E* **86**, 066302.

Canuto, C., Hussaini, M., Quarteroni, A. & Zang, T. 1988 *Spectral methods in fluid dynamics*. Spri-Ver.

Carpenter, M. H. & Kennedy, C. A. 1994 Fourth-order 2n-storage runge-kutta schemes. *Nasa tm* **109112**.

Chaikin, P. M., Lubensky, T. C. & Witten, T. A. 2000 *Principles of condensed matter physics*, , vol. 1. Cambridge Univ Press.

Chen, H., Kandasamy, S., Orszag, S., Shock, R., Succi, S. & Yakhot, V. 2003 Extended boltzmann kinetic equation for turbulent flows. *Science* **301** (5633), 633–636.

Chen, S. & Doolen, G. D. 1998 Lattice boltzmann method for fluid flows. *Annual review of fluid mechanics* **30** (1), 329–364.

Cichowlas, C. & Brachet, M. E. 2005 Evolution of complex singularities in Kida–Pelz and Taylor–Green inviscid flows. *Fluid Dyn. Res.* **36** (4), 239–248.

Davidson, P. 2004 *Turbulence: An introduction for scientists and engineers*. Oxf. Univ. Press, USA.

Dhar, S. K., Sain, A. & Pandit, R. 1997 Inertial-and dissipation-range asymptotics in fluid turbulence. *Physical review letters* **78** (15), 2964–2967.

Donzis, D., Yeung, P. & Sreenivasan, K. 2008 Dissipation and enstrophy in isotropic turbulence: Resolution effects and scaling in direct numerical simulations. *Phys. Fluids* **20** (4), 045108–045108.

Eyink, G. L. & Sreenivasan, K. R. 2006 Onsager and the theory of hydrodynamic turbulence. *Reviews of modern physics* **78** (1), 87.

Frigo, M. & Johnson, S. 2005 The design and implementation of fftw3. *Proc. IEEE* **93** (2), 216–231.

Frigo, M. & Johnson, S. G. 2012 fftw-3.3.3. http://www.fftw.org/doc/, [Online].

Frigo, M. & Johnson, S. G. 2013 fftw. http://www.fftw.org/, [Online].

Frisch, U. 1995 *Turbulence: The Legacy of AN Kolmogorov*. Cambridge University Press, Cambridge, UK.

Frisch, U., Matsumoto, T. & Bec, J. 2003 Singularities of Euler flow? not out of the blue! *J. Stat. Phys.* **113** (5), 761–781.

Germano, M. 1992 Turbulence: the filtering approach. *J. Fluid Mech.* **238** (1), 325–336.

Grafke, T., Homann, H., Dreher, J. & Grauer, R. 2008 Numerical simulations of possible finite time singularities in the incompressible euler equations: comparison of numerical methods. *Physica D: Nonlinear Phenomena* **237** (14), 1932–1936.

Gulak, Y. & Pelz, R. B. 2005 High-symmetry kida flow: Time series analysis and resummation. *Fluid Dyn. Res.* **36** (4), 211–220.

Holm, D. D. & Kerr, R. 2002 Transient vortex events in the initial value problem for turbulence. *Phys. rev. let* **88** (24), 244501.

Hou, T. Y. & Li, R. 2008 Blowup or no blowup? the interplay between theory and numerics. *Physica D: Nonlinear Phenomena* **237** (14), 1937–1944.

Kerr, R. M. 1993 Evidence for a singularity of the three-dimensional, incompressible euler equations. *Phys. Fluids* **5**, 1725.

Kida, S. 1985 Three-dimensional periodic flows with high-symmetry. *J. Phys. Soc. Japan* **54** (6), 2132–2136.

Kida, S. & Murakami, Y. 1997 Kolmogorov similarity in freely decaying turbulence. *Phys. Fluids* **30** (7), 2030–2039.

Kraichnan, R. H. 1967 Inertial ranges in two-dimensional turbulence. *Phys. Fluids* **10**, 1417.

Lesieur, M. & Metais, O. 1996 New trends in large-eddy simulations of turbulence. *Annu. Rev. Fluid Mech* **28** (1), 45–82.

Levermore, C. 1996 Moment closure hierarchies for kinetic theories. *J. Stat. Phys.* **83** (5), 1021–1065.

Liepmann, H. 1979 The rise and fall of ideas in turbulence. *Amer. Sci* **67** (2), 221–228.

Lifshitz, L. D. L. . E. M. 1987 *A Course of Theoretical Physics: Fluid Mechanics*.

Lumley, J. & Yaglom, A. 2001 A century of turbulence. *Flow, Turb. and Comb* **66** (3), 241–286.

Moin, P. & Mahesh, K. 1998 Direct numerical simulation: a tool in turbulence research. *Annu. Rev. Fluid Mech.* **30** (1), 539–578.

Moxey, D. & Barkley, D. 2010 Distinct large-scale turbulent-laminar states in transitional pipe flow. *Proc. Nat. Aca. Sci* **107** (18), 8091–8096.

Orlandi, P. & Pirozzoli, S. 2010 Vorticity dynamics in turbulence growth. *Theor. Comp. Fluid Dyn.* **24** (1), 247–251.

Orlandi, P., Pirozzoli, S. & Carnevale, G. 2012 Vortex events in euler and navier–stokes simulations with smooth initial conditions. *J. Fluid Mech* **1** (1), 1–33.

Orszag, S. A. 1971 On the elimination of aliasing in finite-difference schemes by filtering high-wavenumber components. *Journal of the Atmospheric sciences* **28** (6), 1074–1074.

Pelz, R. B. 2001 Symmetry and the hydrodynamic blow-up problem. *J. Fluid Mech.* **444**, 299–320.

Pelz, R. B. 2003 Extended series analysis of full octahedral flow: numerical evidence for hydrodynamic blowup. *Fluid Dyn. Res.* **33** (1), 207–221.

Peng, Y., Liao, W., Luo, L.-S. & Wang, L.-P. 2010 Comparison of the lattice boltzmann and pseudo-spectral methods for decaying turbulence: Low-order statistics. *Computers & Fluids* **39** (4), 568–591.

Pope, S. 2000 *Turbulent flows*. Cambridge Univ Press.

Richardson, L. F. & Chapman, S. 1965 *Weather prediction by numerical process*. Dover publications New York.

Rogallo, R. S. 1981 Numerical experiments in homogeneous turbulence. *Tech. Rep.*. National Aeronautics and Space Administration.

Sah, P. & Ansumali, S. 2012 Panini: A gpu aware array class. http://nvidia.fullviewmedia.com/gtc2012/0517-B-S0428.html, [Online].

Singh, S., Krithivasan, S., Karlin, I. V., Succi, S. & Ansumali, S. 2011 Energy conserving lattice boltzmann models for incompressible flow simulations. *Commun. Comput. Phys* **13**, 603–613.

Sreenivasan, K. 1999 Fluid turbulence. *Rev. Mod. Phys* **71** (2), 383–395.

Sreenivasan, K. R. & Antonia, R. A. 1997 The phenomenology of small-scale turbulence. *Annu. Rev. Fluid Mech.* **29** (1), 435–472.

Succi, S. 2001 *The lattice Boltzmann equation for fluid dynamics and beyond*. Oxf. Univ. Press, USA.

Thantanapally, C., Patil, D. V., Succi, S. & Ansumali, S. 2013 Universal mechanism for saturation of vorticity growth in fully developed fluid turbulence. *Journal of Fluid Mechanics* **728**, R4.

Toschi, F. & Bodenschatz, E. 2009 Lagrangian properties of particles in turbulence. *Annu. Rev. Fluid Mech.* **41**, 375–404.

Tsinober, A., Shtilman, L. & Vaisburd, H. 1997 A study of properties of vortex stretching and enstrophy generation in numerical and laboratory turbulence. *Fluid. Dyn. Res* **21** (6), 477–494.

Williamson, J. 1980 Low-storage runge-kutta schemes. *J. Comp. Phys.* **35** (1), 48–56.

Yu, D. & Girimaji, S. 2005 Dns of homogenous shear turbulence revisited with the lattice boltzmann method. *Journal of Turbulence* (6).

Yu, D. & Girimaji, S. S. 2006 Multi-block lattice boltzmann method: Extension to 3d and validation in turbulence. *Physica A: Statistical Mechanics and its Applications* **362** (1), 118–124.

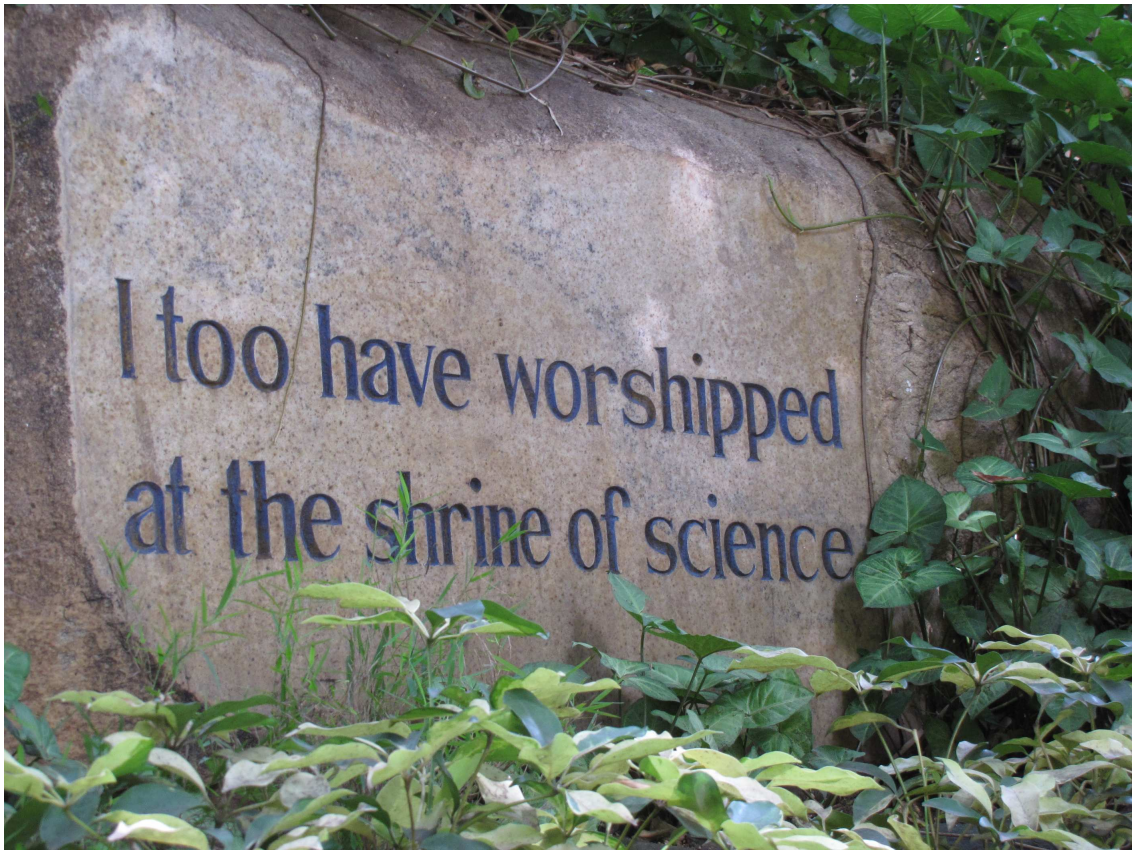
I too have worshipped
at the shrine of science